ANALYSIS OF THE SURFACE DEFORMATION CAUSED BY THE HATAY EARTHQUAKE ON FEBRUARY 20, 2023 WITH InSAR TECHNIQUE

by

Merve ERCAN

B.S., Geomatics Engineering , Erciyes University, 2019

Submitted to the Kandilli Observatory and Earthquake
Resarch Institute in partial fulfillment of
the requirements for the degree of
Master of Science

Graduate Program in Geodesy

Boğaziçi University

2024

ANALYSIS OF THE SURFACE DEFORMATION CAUSED BY THE HATAY EARTHQUAKE ON FEBRUARY 20, 2023 WITH InSAR TECHNIQUE

APPROVED BY:

Assist. Prof. Tülay KAYA EKEN (Thesis Supervisor)	.....
Prof. Dr. Haluk ÖZENER	.....
Assoc.Prof. Muharrem Hilmi ERKOÇ	.....

DATE OF APPROVAL: 24.07.2024

ACKNOWLEDGEMENTS

I would like to thank my dear father Cumhur ERCAN who has always supported and embraced me in this thesis and at every point of my life, my dear mother Fatma ERCAN whose hand I always see on my shoulder and whose touch has turned my life into a flower garden, and my dear brothers Rahmican and Mustafa ERCAN. I am very happy for your existence, I love you very much.. I would like to thank my dear advisor Assoc. Prof. Dr. Tülay KAYA EKEN who approached me with patience and interest throughout the implementation of this thesis, who was with me at every stage from the beginning to the end of my thesis and throughout my graduate career, who guided me and ensured that I had a good academic career, who left an impact not only in academia but also in every point of my life. I would also like to express my gratitude to my dear teacher Prof. Dr. Haluk ÖZENER who has always supported me throughout my academic career, guided my development, introduced me to Kandilli and made me feel that he was always with me like a father. I would like to pay my respects to the late Prof. Dr. Onur GÜRKAN, who passed away in 2023, who trained many scientists, was one of the most important names in the world of science and geodesy, and changed the direction of my career. I am grateful to my department professors who supported me to progress in the light of science and to my dear department friend Research Assistant Çağkan Serhun ZOROĞLU, with whom I have shared many things in the last three years. I would also like to thank my friends Julay YAMAÇ, Cansu-Murat DÜZ and Mustafa ARSLAN, who have always been by my side and never withheld their support. It is a good thing that you exist and continue to exist. I would also like to thank Kayseri Metropolitan Municipality GIS Branch Manager Fatih HAREKET and my valuable colleagues Ali, Metin, Yusuf, Tuğba, Nuh and Turan Bey. I would also like to thank KASKİ General Directorate GIS Branch Manager Abdullah KARAGÖZ and my valuable colleagues Miraç, Mustafa, Neriman and Hayri Bey for their patience and understanding during this process.

ABSTRACT

ANALYSIS OF THE SURFACE DEFORMATION CAUSED BY THE HATAY EARTHQUAKE ON FEBRUARY 20, 2023 WITH InSAR TECHNIQUE

The tectonic of Türkiye are mainly shaped by the movements of the surrounding tectonic plates. The Arabian and African plates move northward against the Anatolian and Eurasian plates, influencing the tectonic dynamics of Türkiye. The Anatolian Plate is moving predominantly to the west and southwest, and this movement is accommodated by the North Anatolian Fault Zone (NAFZ) with right-lateral strike-slip motion and the East Anatolian Fault Zone (EAFZ) with left-lateral strike-slip motion. Further south, the movement continues along the Dead Sea Fault Zone (DSFZ) in southeastern Türkiye. On February 20, 2023, an earthquake with magnitude of Mw 6.3, known as the Hatay earthquake, occurred at the intersection of the EAFZ, the DSFZ, and the onshore extension of the Cyprus Arc, two weeks after the Kahramanmaraş earthquakes of February 6, 2023. The DSFZ, trending north-south, originates south of the EAFZ and extends across Syria, Lebanon, and Israel. Although the fracture segment near Hatay is not as active as the northern parts of the EAFZ, it has experienced significant seismic activity in the past. Interferometric Synthetic Aperture Radar (InSAR) method was used on Sentinel-1 data to assess the deformation caused by the Hatay earthquake. The TopsApp module within the InSAR Scientific Computing Environment (ISCE) software was utilized to analyze the SAR images acquired before and after both earthquakes. This analysis focused on obtaining interferograms of the co-seismic deformation in the Hatay region from both ascending and descending satellite tracks. Our data analysis indicates that the maximum amount of deformation caused by the 2023 Hatay earthquake is $\sim$ 17 cm.

ÖZET

InSAR VERİ ANALİZİNDEN ÇIKARILAN 2023 HATAY DEPREMİNİN YÜZEY DEFORMASYONU VE KAYNAK PARAMETRELERİ

Türkiye'nin tektonik özellikleri temel olarak çevresindeki tektonik plakaların hareketleriyle şekillenmektedir. Arap ve Afrika levhaları, Anadolu ve Avrasya levhalarına göre kuzeye doğru hareket ederek Türkiye'nin tektonik dinamiklerini etkilemektedir. Anadolu Levhası ağırlıklı olarak batı ve güneybatıya doğru hareket etmekte ve bu hareket sağ yanal çarpma-kayma hareketine sahip Kuzey Anadolu Fay Zonu (KAFZ) ve sol yanal çarpma-kayma hareketine sahip Doğu Anadolu Fay Zonu (DAFZ) tarafından karşılanmaktadır. Daha güneyde, hareket Türkiye'nin güneydoğusundaki Ölü Deniz Fay Zonu (ÖDFZ) boyunca devam etmektedir. 20 Şubat 2023 tarihinde, 6 Şubat 2023 Kahramanmaraş depremlerinden iki hafta sonra, KAFZ, DAFZ ve Kıbrıs Yayı'nın karadaki uzantısının kesiştiği noktada Hatay depremi olarak bilinen Mw 6.3 büyüklüğünde bir deprem meydana gelmiştir.Kuzey-güney doğrultusunda uzanan ÖDFZ, DAFZ'nin güneyinden başlayarak Suriye, Lübnan ve İsrail boyunca uzanmaktadır. Hatay yakınlarındaki kırık segmenti, DAFZ'nin kuzey kesimleri kadar aktif olmasa da, geçmişte önemli sismik aktiviteler yaşamıştır. Kahramanmaraş ve Hatay depreminin neden olduğu deformasyonu değerlendirmek için Sentinel-1 verileri üzerinde İnterferometrik Sentetik Açıklıklı Radar (InSAR) yöntemi kullanılmıştır. InSAR Scientific Computing Environment (ISCE) yazılımı içindeki TopsApp modülü, her iki depremden önce ve sonra elde edilen SAR görüntülerini analiz etmek için kullanılmıştır. Bu analiz, Hatay bölgesindeki eş-sismik deformasyonun hem yükselen hem de alçalan uydu izlerinden interferogramlarının elde edilmesine odaklanmıştır. Veri analizimiz, 2023 Hatay depreminin neden olduğu maximum deformasyon miktarının ∼17 cm olduğunu göstermektedir.

TABLE OF CONTENTS

ACKNOWLEDGEMENTS iii
ABSTRACT iv
ÖZET v
LIST OF FIGURES vii
LIST OF TABLES xii
LIST OF SYMBOLS xiii
LIST OF ACRONYMS/ABBREVIATIONS xiv
1. INTRODUCTION 1
1.1. Tectonic Background 3
1.2. East Anatolian Fault 7
1.3. Historical Earthquakes 13
2. METHODOLOGY AND DATA ANALYSIS 17
2.1. SAR Interferometry 17
2.1.1. Steps for InSAR analysis using TopsApp in ISCE2 22
2.2. DATA Set 24
2.3. Co-Seismic Deformation 25
2.4. Interferograms Generation 26
2.5. Tropospheric Correction 31
2.5.1. Converting zenith tropopsheric delay to slant phase delay 32
2.5.2. InSAR Tropospheric Phase Delay (slant) 33
2.6. HypoDD 42
3. DISCUSSION 44
4. CONCLUSION 46
REFERENCES 48

LIST OF FIGURES

Figure 1.1. The prominent tectonic features surrounding the Anatolian Plate. Below is an analysis of the essential components: The Anatolian Plate refers to the central section of the map. The Eurasian Plate forms the northern boundary of the Anatolian Plate. The African Plate is located on the southern border of the map. The Arabian Plate forms the southeastern boundary of the Anatolian Plate. (adapted from Okay et al., 2000; GPS velocity values taken from Reilinger et al., 2006) 1

Figure 1.2. Anatolia's regional tectonic map. The plate borders are represented by the green lines, while the velocity vectors of the Anatolia and Arabian plates relative to the Eurasian Plate are indicated the white arrows. Volcanoes are represented as pink triangles with openings called vents. Mm: Marmara Region (near the Marmara Sea) Po: Pontides (mountain range in northern Türkiye) Cd: Central Anatolian Block (a part of the Anatolian Plate) Ta: Taurus Mountains (a mountain range in southern Türkiye) Xp: Lesser Caucasus (mountain range in the Caucasus region) (Legendre et al., 2020) 4

Figure 1.3. Figures a and b depict the tectonic and geological features of the Eastern Mediterranean region, specifically the area around the junction of the African, Arabian, and Anatolian plates. (Karabacak et al., 2010) 6

Figure 1.4. The map shows the tectonic setting of the region around Türkiye, focusing on the interactions between the Eurasian Plate, Arabian Plate, African Plate, and the Anatolian Block. Major fault lines, plate boundaries, and recent significant earthquakes are highlighted. 2023 M7.5: A magnitude 7.5 earthquake indicated by a blue star along the East Anatolian Fault. 2023 M7.8: A magnitude 7.8 earthquake indicated by an orange star along the East Anatolian Fault.(Irina-Marilena Stanciu et al.,2023) 8

Figure 1.5. Map showing the segments of the East Anatolian Fault Zone and associated seismic hazards. (Arpat, 1971; Arpat ve Şaroğlu, 1972; Seymen ve Aydın, 1972; Ambraseys, 1988; Ambraseys ve Jackson, 1998; Çetin vd., 2003; Herece, 2008; Karabacak vd., 2011; Duman ve Emre, 2013) 10

Figure 1.6. The map illustrates the intricate plate structure and triple junctions that characterize the region, including the Anatolian Plate, Arabian Plate, and Sinai Plate. It highlights significant fault lines and tectonic junctions. EAF: East Anatolian Fault KTJ: Karlıova Triple Junction KOF: Kabataş Osmaniye Fault HTJ: Hatay Triple Junction KF: Karasu Fault AT: Amanos Thrust GT: Göksun Thrust CE: Çelikhan Fault YF: Yumurtalık Fault CA: Cyprus Arc DSF: Dead Sea Fault(Özkan et.al.,2003) 12

Figure 1.7. This illustration represents the tectonic context and past occurrence of earthquakes in eastern Türkiye, emphasizing several fault lines and notable seismic events. NAFZ : North Anatolian Fault Zone EAFZ : East Anatolian Fault Zone DSFZ : Dead Sea Fault Zone CSF : Central Segment of the Fault C-CAEFZ : Central-East Anatolian Fault Zone ÇSF : Çardak-Sürgü Fault ER : Erzincan K : Karlıova EL : Elazığ MA : Malatya DB : Diyarbakır SU : Şanlıurfa AY : Adıyaman GA : Gaziantep AD : Adana AN : Antakya Ç : Çelikhan GÖ : Gölbaşı P : Pazarcık N : Nurhak E : Elbistan G : Göksun T : Türkoğlu Kr : Kırıkhan AB : Amik Basin GB : Ghab Basin (Alka Tripathy-Lang,2023) 16

Figure 2.1. This diagram depicts the principle of using satellite-based Interferometric Synthetic Aperture Radar (InSAR) to measure ground movement. The demonstration illustrates the capability of satellites to identify alterations in the Earth's surface over a period of time by analyzing two radar pictures captured at distinct moments. (www..volcano.si.edu) 19

Figure 2.2. This figure depicts the InSAR image. The concentric circles (fringes) and variations in the image signify the magnitude and pattern of surface displacement over a period of time. (Figure by NASA) . . 21

Figure 2.3. This figure shows the study area. 24

Figure 2.4. Ascending wrapped interferogram obtained from the analysis of frame 114 SAR data to investigate the deformation due to the Hatay earthquake. 28

Figure 2.5. Ascending unwrapped interferogram obtained from the analysis of frame 114 SAR data to investigate the deformation due to the Hatay earthquake. 29

Figure 2.6. Descending wrapped interferogram obtained from the analysis of frame 471 SAR data to investigate the deformation due to the Hatay earthquake. 30

Figure 2.7. Descending unwrapped interferogram obtained from the analysis of frame 471 SAR data to investigate the deformation due to the Hatay earthquake. 31

Figure 2.8. The Ascending data the zenith delays for two distinct dates: February 21, 2023 (Secondary) and February 9, 2023 (Reference). . . . 33

Figure 2.9. Reference and secondary slant phase delays. The labels indicate the dates of the radar acquisitions used in the InSAR analysis. The secondary image was acquired on February 21, 2023, and the reference image on February 9, 2023. 34

Figure 2.10. The provided image is a differential interferogram showing the "Differential phase delay (20230209-20230221) [rad]." This map represents the phase difference between radar images acquired on February 9, 2023, and February 21, 2023. 35

Figure 2.11. The unwrapped interferogram is presented both before and after application of the APS correction to the ascending data. 36

Figure 2.12. The APS correction cross-sections taken along profiles 1 to 4 shown in Figure 2.11. 37

Figure 2.13. The provided image consists of two maps showing "Secondary zenith delay [m]: 20230222" and "Reference zenith delay [m]: 20230210." 38

Figure 2.14. Reference and secondary slant phase delays for descending data. The labels indicate the dates of the radar acquisitions used in the InSAR analysis. The secondary image was acquired on February 22, 2023, and the reference image on February 10, 2023. 39

Figure 2.15. Differential phase delay between radar images taken on February 10, 2023 and February 22, 2023 (descending orbit). 40

Figure 2.16. The unwrapped interferogram is presented both before and after application of the APS correction to the descending data. 40

Figure 2.17. The APS correction cross-sections taken along profiles 1 to 4 shown in Figure 2.16. 41

Figure 2.18. Aftershock distribution of Kahramanmaraş earthquakes (Özener et al., EGU2023) processed with HypoDD technique (Waldhauser and Elsworth, 2000). Letters on the map indicate the locations of the cross sections. Depth sections of the relocated earthquake distribution along the profiles in Hatay region are also given. . . . 43

LIST OF TABLES

Table 1.1. Earthquakes that occurred on the EAFZ between MS17 and 1900 (KOERI earthquake catalog) 13

Table 1.2. Earthquakes that occurred on the EAFZ between 1900 and 2005 (KOERI earthquake catalog 14

Table 1.3. Earthquakes that occurred on the EAFZ between 2005 and 2023 (KOERI earthquake catalog) 14

Table 2.1. SAR frequency bands 20

LIST OF SYMBOLS

$\mathbf{M}$	Magnitude
M	Average magnitude of the earthquake catalogue
$\mathbf{M_0}$	Seismic Moment
$\mathbf{M_w}$	Moment magnitude
$\mathbf{N}$	Number of earthquakes
$\mathbf{n}$	Number of sites
$\mathbf{r}$	Station position vector
$\mathbf{R}$	Rotation matrix to local coordinate system
$\mathbf{t_k}$	Step size
$\mathbf{v_1}$	Velocity vector
$\mathbf{v_2}$	Velocity vector
$\mathbf{x} \times \mathbf{y}$	Vector product operator
$\mathbf{x}^{(k)}$	Original point
$\mathbf{x}^{(k+1)}$	Point
$t_1 1$	Time interval
α	Blending parameter or scale
$\beta_t(i)$	Backward variable
Θ	Parameter set
σ^2	Variance factor
μ	Shear modulus

LIST OF ACRONYMS/ABBREVIATIONS

NAFZ	North Anatolian Fault Zone
EAFZ	East Anatolian Fault Zone
DSFZ	Dead Sea Fault Zone
CSF	Central Segment of the Fault
C-CAEFZ	Central-East Anatolian Fault Zone

1. INTRODUCTION

The Earth's crust exhibits a complex structure. Tectonically induced displacements, ranging from milliseconds to years and from millimeters to meters on both local and global scales, are linked to plate tectonics and the seismic cycle (Thatcher, et al.,2006). Therefore, the comprehensive analysis of the complex structure of active faults has an important place in the field of earth sciences. Especially, in regions prone to frequent seismic activity, such as Türkiye, which is located in a region of active faults and high seismicity for centuries (Figure 1.1), an accurate understanding of crustal movements, fault dynamics and surface deformations is of utmost importance.



Figure 1.1. The prominent tectonic features surrounding the Anatolian Plate. Below is an analysis of the essential components: The Anatolian Plate refers to the central section of the map. The Eurasian Plate forms the northern boundary of the Anatolian Plate. The African Plate is located on the southern border of the map. The Arabian Plate forms the southeastern boundary of the Anatolian Plate. (adapted from Okay et al., 2000; GPS velocity values taken from Reilinger et al., 2006)

Figure 1.1. represents the key features that influence this complex structure in Türkiye; the North Anatolian Fault (NAF) is a significant fault line that extends across the northern region of Türkiye, characterized by horizontal movement along its fault plane. The boundary between the Eurasian Plate and the Anatolian Plate is demarcated by it. The East Anatolian Fault (EAF) is a prominent strike-slip fault located in eastern Türkiye. It serves as a boundary between the Anatolian Plate and the Arabian Plate. The Hellenic Arc is a subduction zone located southwest of the Anatolian Plate, where the African Plate is being forced beneath the Anatolian Plate. The Cyprus Arc is a tectonic boundary where the African Plate and the Anatolian Plate come into contact. The Mediterranean Ridge is situated south of the Anatolian Plate and is closely linked to the intricate tectonic activity in the area. The Dead Sea Transform is a significant transform fault that extends along the boundary between the Arabian Plate and the African Plate. The Bitlis-Zagros Fold and Thrust Belt is a geologic zone characterized by significant tectonic compression and deformation resulting from the collision between the Arabian Plate and the Eurasian Plate.

Recently, both Global Navigation Satellite System (GNSS) and Interferometric Synthetic Aperture Radar (InSAR) data have been used together to analyze crustal deformation, improving the accuracy and clarity of assessments and predictions of current and potential future natural disasters.

The significance of satellite-based geodetic measurement techniques for geohazard assessment has increased considerably over the past two decades. This is due to the increased demand for satellite observations, which enable for more comprehensive analysis and provide rapid, precise, and easily understandable results on surface deformation. Remote sensing data, particularly high-resolution Synthetic Aperture Radar (SAR) imagery, is used at various stages of the disaster management due to its ability to continuously monitor surface deformation of large remote and inaccessible areas at regular intervals with precise measurements (Joyce et al., 2009). Therefore, the importance of satellite geodesy is increasing on a daily basis in this context.

The InSAR technique was first used in the 1992 Landers (California) earthquake and demonstrated its effectiveness in determining surface deformation (Massonnet et al., 1993; Zebker et al., 1994). Subsequently, InSAR data processing has been frequently employed to observe the movement of the Earth's crust in conjunction with surface deformation resulting from earthquakes. During this process, both pre- and post-earthquake SAR images are utilized. The most crucial criterion in the processing of InSAR data is the selection of appropriate images. An interferogram is then extracted from these images, which represents the difference between the images and the deformation of the Earth's crust.

The objective of this thesis is to provide a comprehensive analysis of the surface deformation in the Hatay region resulting from the 6 February 2023 Kahramanmaraş and 20 February 2023 Hatay earthquakes, which occurred along the East Anatolian Fault zone in eastern Türkiye using InSAR data.

1.1. Tectonic Background

Türkiye is situated within the Alpine-Himalayan orogenic system, which is formed by the convergence of several tectonic plates (Figure 1.1). The relative movements of the surrounding Eurasian, African, and Arabian plates with the Anatolian Plate make the tectonic structure of Türkiye highly complex and dynamic.(Figure 1.2) The northward movement of the Arabian Plate relative to the Eurasian Plate and the subduction of the African Plate under the Anatolian Plate resulted in collision in eastern Türkiye, which caused the Anatolian Plate to compress and rotate counterclockwise on its western edge.



Figure 1.2. Anatolia's regional tectonic map. The plate borders are represented by the green lines, while the velocity vectors of the Anatolia and Arabian plates relative to the Eurasian Plate are indicated the white arrows. Volcanoes are represented as pink triangles with openings called vents. Mm: Marmara Region (near the Marmara Sea) Po: Pontides (mountain range in northern Türkiye) Cd: Central Anatolian Block (a part of the Anatolian Plate) Ta: Taurus Mountains (a mountain range in southern Türkiye) Xp: Lesser Caucasus (mountain range in the Caucasus region) (Legendre et al., 2020)

The relative motions between these plates have resulted in significant seismic activity and deformation across the region along the active fault systems. The two transform fault systems of Türkiye have also been formed in under this tectonic setting. These are the North Anatolian Fault Zone (NAFZ) and East Anatolian Fault Zone (EAFZ), which exhibit right-lateral and left-lateral strike-slip faulting mechanisms, respectively (Ketin, 1948; Arpat and Saroglu, 1971). Türkiye has experienced high frequency of earthquakes of varying magnitudes, which is indicative of the ongoing tectonic activity in the region (Sengor and Yilmaz, 1981).

The study area, Hatay, is located in the south of Türkiye, between 35°52'-37°4' latitudes and 35°40'-36°35' longitudes. Hatay is bordered by Osmaniye to the north, Adana to the northwest and Gaziantep to the northeast. It borders the Mediterranean Sea to the west and Syria to the south and east. This city is placed in a region affected by the complex tectonic interactions of the Arabian, African and Eurasian plates. This tectonic setting creates a dynamic environment where multiple faults and seismic zones converge. The prominent features affecting Hatay are the two transform fault systems, the Dead Sea Fault (DSF) Zone and the EAFZ. It is also surrounded by diverse geographical and geological features. Encircled by the Amanos Mountain Range, Hatay exhibits strike-slip faults, and it encompasses the fertile Amik Plain, classified as a 1st degree earthquake zone due to its alluvial soil and proximity to significant fault lines such as the DSF Zone, EAFZ, and Cyprus Arc (Figure 1.3). Throughout its history, both before and after 1900, Hatay and its surrounding provinces have experienced large and destructive earthquakes, causing considerable damage. The DSF system, extending from the Red Sea to Türkiye via Lebanon and Syria, accommodates movement between the Arabian and African plates, contributing to the seismic activity in the region. Hatay also experiences tectonic stresses associated with the collision between the Arabian Plate and the Eurasian Plate, which leads to uplift and deformation. Hatay's complex tectonic structure leads to increased seismic risk, and since earthquakes are a recurrent natural disaster in the region, understanding and monitoring these tectonic processes is vital for assessing seismic hazards in Hatay and implementing effective mitigation strategies.

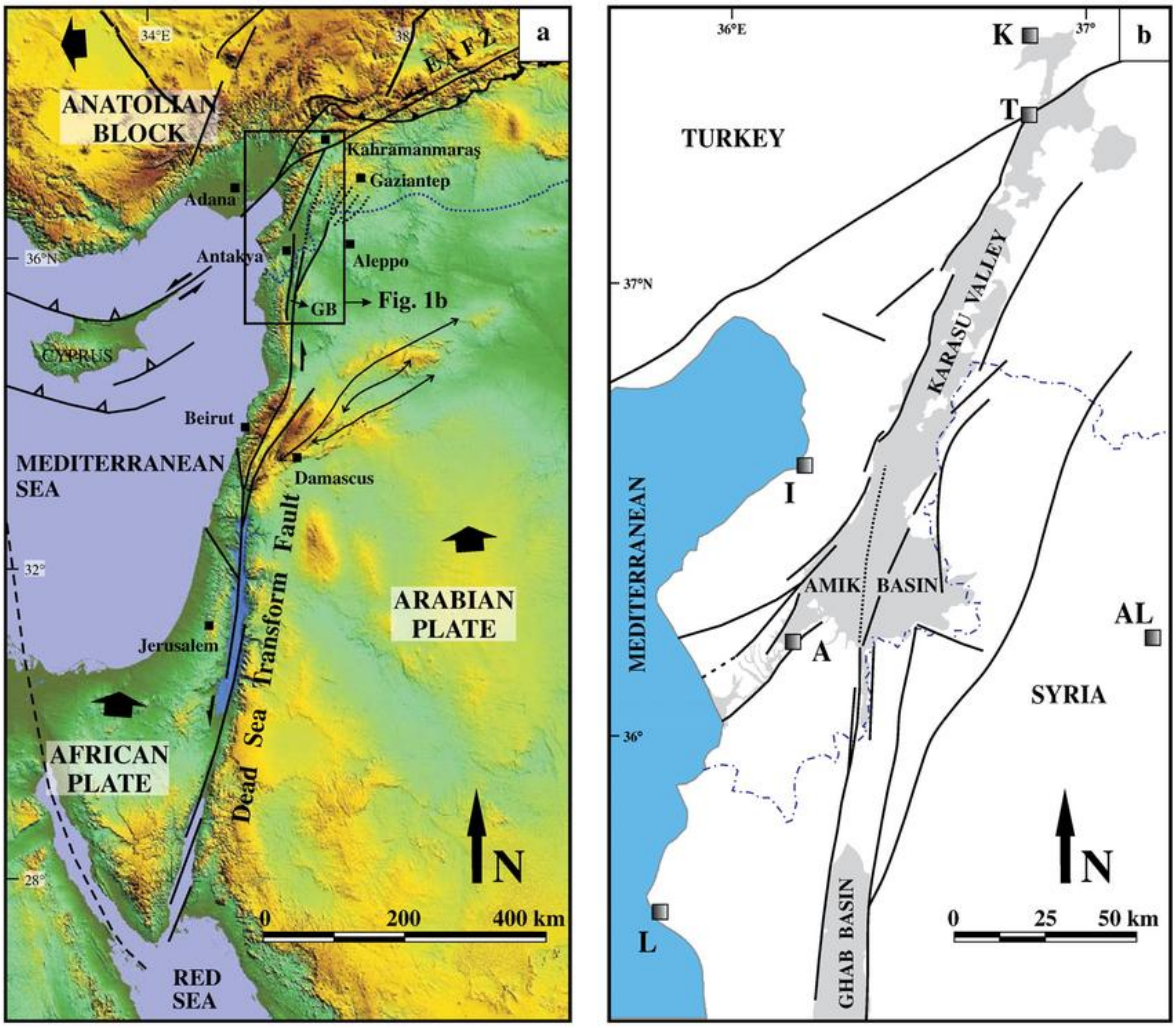

Figure 1.3. Figures a and b depict the tectonic and geological features of the Eastern Mediterranean region, specifically the area around the junction of the African, Arabian, and Anatolian plates. (Karabacak et al., 2010)

The integrated data from Panels (a) and (b) in Figure 1.3. offer a comprehensive account of the tectonic and geographical characteristics of the region. Panel (a) provides an overview of the region's geographical context, encompassing a vast area spanning Türiye, Syria, Lebanon, Israel, Jordan, Egypt, and Cyprus. It identifies significant tectonic features, including the DSTF which is a major fault line that stretches from the Red Sea, passing through the Dead Sea area, and continuing northwards beyond Jerusalem and Damascus; the EAF, which is situated at the northern edge of the Arabian Plate, in close proximity to Kahramanmaraş and Gaziantep in Türkiye,

and various topographic gradients indicative of altitude differences. Furthermore, the region's major urban centers, including Antakya, Aleppo, Damascus, and Beirut, are identified as significant urban hubs within this expansive region. Panel (b) provides a detailed examination of specific areas, such as the Karasu Valley and Amik Basin in southern Türkiye and northern Syria. It offers a comprehensive account of the geological formations and various fault lines present in these regions. Although the map does not include specific elevation data, it does feature latitude and longitude markers for precise location references, thus enhancing its utility for geological studies and spatial analysis in the region.

InSAR, a technique of great importance for surface deformation analysis and the tectonic structure of the Earth's crust, has been a fundamental tool for two decades. GNSS measurements, when combined with InSAR analysis, remain the most effective methods for the analysis of earthquakes. Therefore, researchers engaged in seismic studies frequently integrate findings derived from GPS velocity measurements and InSAR data. This thesis will both InSAR rates in order to obtain the most precise assessment of surface deformation. Furthermore, the use of both ascending and descending InSAR data setqs will enable a comparative evaluation of the deformation caused by the Hatay earthquakes.

1.2. East Anatolian Fault

The East Anatolian Fault (EAF) is the second most active fault zone in Türkiye, spanning approximately 550 km in length. It is situated in eastern Türkiye and runs from the northern end of the Dead Sea Fault Zone (DSFZ) to the North Anatolian Fault Zone (NAFZ) near the Karlıova Triple Junction on the Anatolian Plate (Figure 1.4). The route primarily follows a northeast-southwest direction in eastern Anatolia, traversing many provinces like Gaziantep, Kahramanmaraş, Adıyaman, Malatya, Elazığ, and Bingöl. The fault zone extends in a southeastern direction into the Syrian border area, where it undergoes a change into different geological features. The has substantial seismic activity and serves as a crucial conduit for accommodating tectonic

movement between the Eurasian and Arabian Plates in this region of Türkiye.

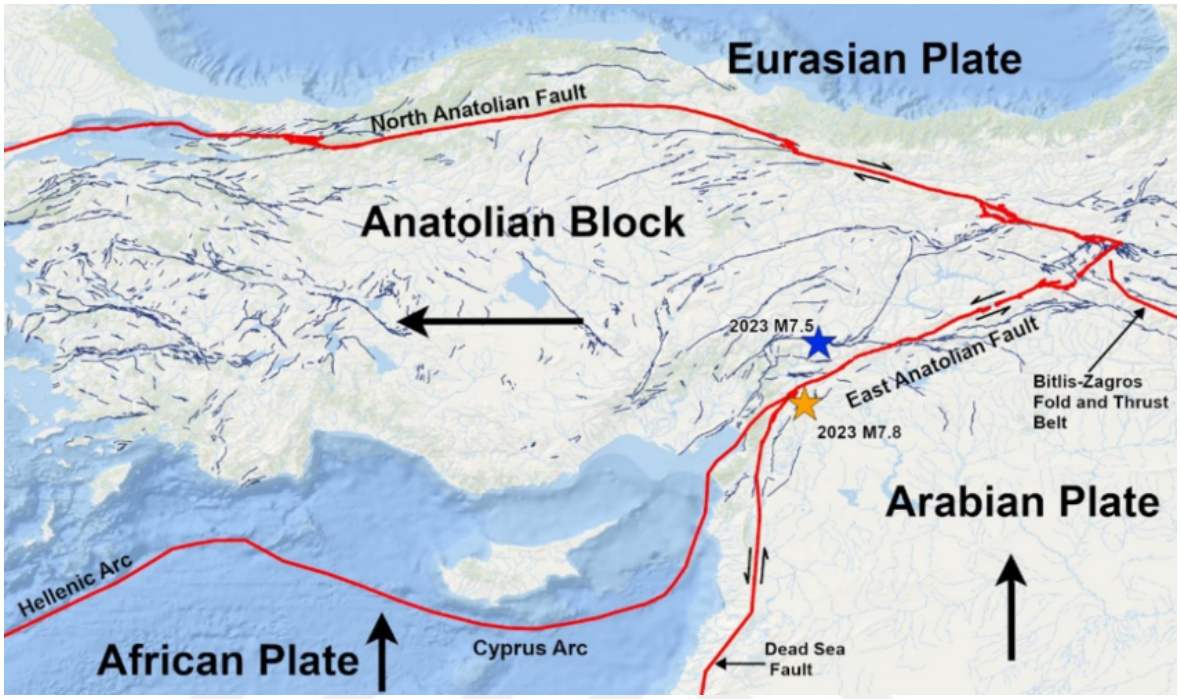

Figure 1.4. The map shows the tectonic setting of the region around Türkiye, focusing on the interactions between the Eurasian Plate, Arabian Plate, African Plate, and the Anatolian Block. Major fault lines, plate boundaries, and recent significant earthquakes are highlighted. 2023 M7.5: A magnitude 7.5 earthquake indicated by a blue star along the East Anatolian Fault. 2023 M7.8: A magnitude 7.8 earthquake indicated by an orange star along the East Anatolian Fault.(Irina-Marilena Stanciu et al.,2023)

Though it is clear that the collision between the Arabian and Anatolian plates has led to compression in eastern Türkiye, resulting in the formation of the East and North Anatolian faults (Sengör, 1980), the connections and inferences regarding the fault systems in Türkiye's geological framework vary across different studies. Some studies suggest that the EAFZ is connected to the DSF (e.g. McKenzie 1976; Gülen et al. 1987; Karig and Kozlu 1990; Perinçek and Çemen 1990; Westaway Arger 1996; Westaway 2003, Khalifa et al., 2018). Some researchers have suggested that the Amanos Fault may be a part of the EAF, extending between Karlıova and the Amik Triple junction (Arpat and Saroğlu, 1972, 1975; Saroğlu et al., 1992a, b; Herece, 2008; Karabacak

et al., 2010). Additionally, some studies estimate the age of Eastern Anatolia to be 4-5 million years (Perinçek et al., 1987). Some researchers note a lateral displacement of 15-25 km and a displacement rate of 5 mm per year for the EAFZ, which is also estimated to be 4-5 million years old (Gülün et al., 1987). Pirazzoli et al. (1993) suggest that the fault lines of the EAF system were reactivated approximately 1500 years ago. The observable deformation and elevation changes in the coastlines around the Antakya region have been occurring since the Pleistocene, A review of historical records also indicates an increase in seismic activity along the EAFZ in recent times, as evidenced by the recent earthquakes in the vicinity of the EAFZ.

The EAF system is comprised of six distinct segments (Figure 1.5). The segments are as follows:

- Karlıova – Bingöl Segment: This segment is approximately 65 km long. It is in NE direction.

- The Palu–Caspian Segment: This segment is approximately 50 km long and has a NE direction.

- The Hazar–Sincik segment: This segment is approximately 85 km long. It is in NE direction. It consists of two more sub-segments.

(The northern segment is located between Hazar Lake and Doğanyol. The southern segment is located between Doğanyol and Sincik.)

- The Çelikhan-Gölbaşı segment: This segment is approximately 50 km long and has an NE direction.

- The Gölbaşı-Türkoğlu segment: This segment is approximately 90 km long and has an NE direction.

- Turgölu – Antakya Segment: This segment is approximately 145 km long and has an NE direction.

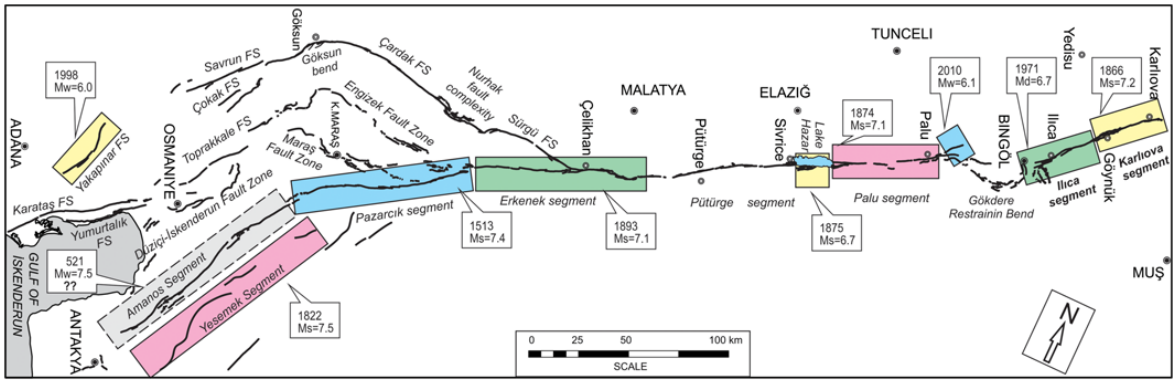

Figure 1.5. Map showing the segments of the East Anatolian Fault Zone and associated seismic hazards. (Arpat, 1971; Arpat ve Şaroğlu, 1972; Seymen ve Aydın, 1972; Ambraseys, 1988; Ambraseys ve Jackson, 1998; Çetin vd., 2003; Herece, 2008; Karabacak vd., 2011; Duman ve Emre, 2013)

Fault Segments:

- The map depicts many fault segments along the East Anatolian Fault Zone.

- Every segment is assigned a specific color and name, such as the Amanos Segment, Erkenek Segment, Palu Segment, and Karlıova Segment.

- The fault segments are identified by their corresponding names and distinguished by various colors to enhance clarity.

Geographical References:

- Major cities and towns like Adana, Antakya, Osmaniye, Malatya, Elazığ, Tunceli, and Bingöl are marked for geographical context. Key geographical features and fault zones are labeled, such as the Karataş FS, Yumurtalık FS, Savrun FS, and Göksun FS.

Scale and Orientation:

- The scale bar at the bottom provides a reference for distance, indicating 0 to 100 kilometers.

Explanation of Fault Segments and Historical Earthquakes:

- Amanos Segment: Located near Osmaniye and Antakya. Associated with significant historical earthquakes, including the 1822 Ms=7.5 earthquake.
- Pazarcık Segment: Extends from the Erkenek Fault Zone towards Pazarcık. Historical earthquake 1513 Ms=7.4 is marked along this segment.
- Erkenek Segment: Runs through the Erkenek Fault Zone. The 1893 Ms=7.1 earthquake is noted in this area.
- Palu Segment: Positioned near the towns of Palu and Sivrice. Historical earthquakes include 1874 Ms=7.1 and 1875 Ms=6.7.
- Karlıova Segment: Located in the eastern part near Bingöl and Karlıova. Historical events include the 1866 Ms=7.2 earthquake.

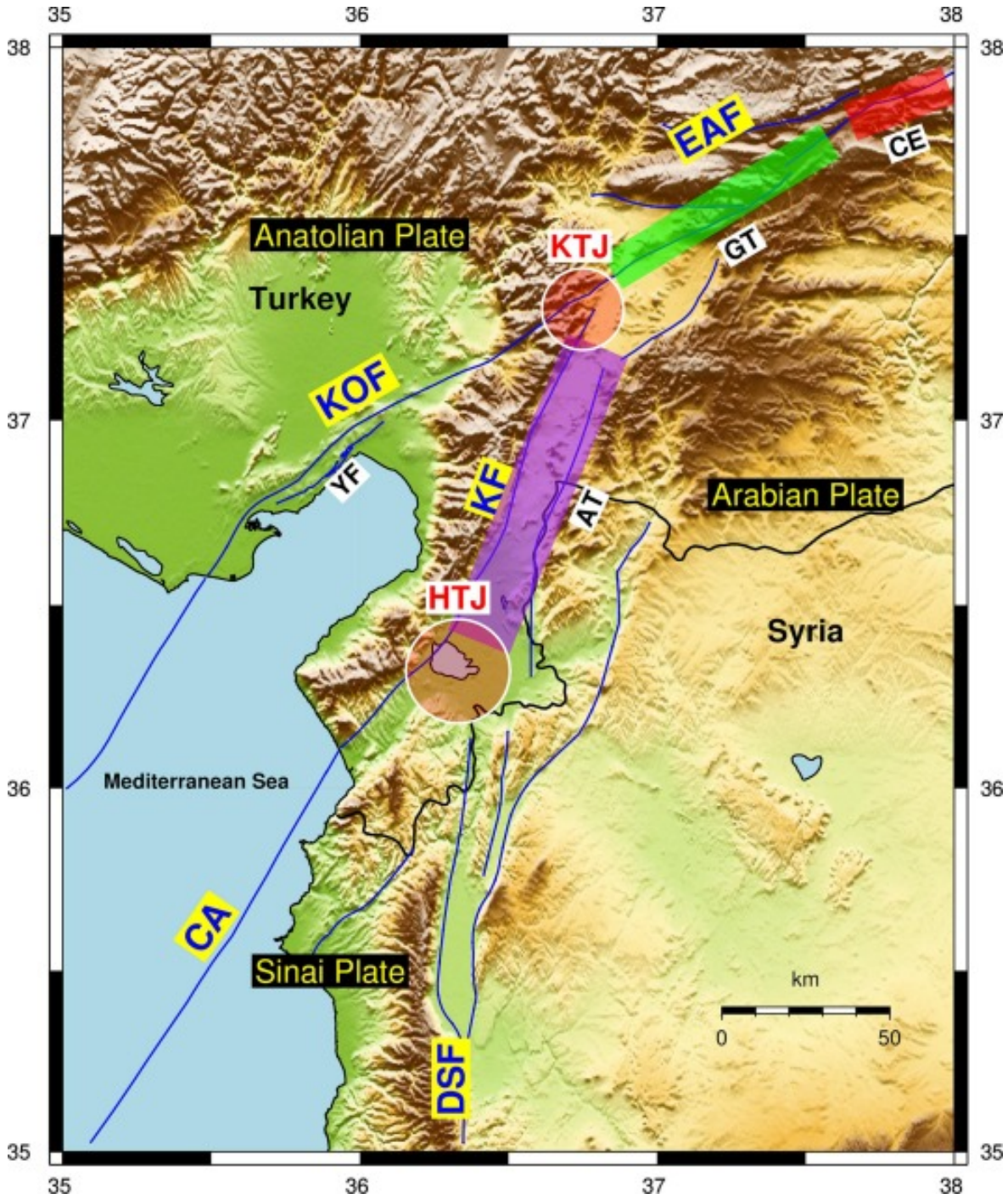

Figure 1.6. The map illustrates the intricate plate structure and triple junctions that characterize the region, including the Anatolian Plate, Arabian Plate, and Sinai Plate. It highlights significant fault lines and tectonic junctions. EAF: East Anatolian Fault KTJ: Karlıova Triple Junction KOF: Kabataş Osmaniye Fault HTJ: Hatay Triple Junction KF: Karasu Fault AT: Amanos Thrust GT: Göksun Thrust CE: Çelikhan Fault YF: Yumurtalık Fault CA: Cyprus Arc DSF: Dead Sea Fault(Özkan et.al.,2003)

1.3. Historical Earthquakes

The East Anatolian Fault (EAF) Zone has a long and distinguished history, marked by a number of significant earthquakes due to its dynamic tectonic activity and impact on the eastern region of Türkiye. The fault system has been responsible for a series of seismic events that have had a significant impact over the centuries. This historical process started with the catastrophic1822 Antakya earthquake, was followed by a series of significant tremors in 1866, 1872, 1874, 1875, 1893, and culminated with the 1905 Malatya earthquake (Data sources KOERI earthquake catalog). The EAF comprises a number of distinct sections, each exhibiting a unique set of characteristics that contribute to the formation of different earthquake patterns with varying slip rates. The recurrence interval of earthquakes along this fault zone is estimated to range from 300 to 600 years. For example, segments such as Karlıova - Bingöl have produced large earthquakes at frequent intervals and caused considerable damage (Ambraseys, N.N., 1989). On the other hand, there are segments that were ruptured by a single earthquake, such as the 145 km long Turkoglu - Antakya segment. Some segments, such as the Göllübaşı – Turkoğlu segment, can remain seismically inactive for long periods of time, creating seismic gaps lasting 495 to 894 years. The historical earthquakes along the EAF, as presented in the tables below, indicate ongoing seismic activity and its potential impact on the region.

DATE	LATITUDE	LONGITUDE	Ms	LOCATION
29.11.1114	37,5	37,5	7.8	Kahramanmaraş
22.01.1544	38	37	6	Elbistan
28.05.1789	38,8	39,5	7	Elazığ
13.08.1822	36,7	36,5	7.5	Antakya
12.05.1866	39,2	41	7.2	Göynük
03.04.1872	36,4	36,4	7.2	Amik
27.03.1875	38,5	39,5	6.7	Hazar
02.03.1893	38	38,3	7.1	Malatya

Table 1.1. Earthquakes that occurred on the EAFZ between MS17 and 1900 (KOERI earthquake catalog)

DATE	LATITUDE	LONGITUDE	Ms	LOCATION	LOST LIFE
12.04.1905	39	39	6.8	Pütürge-MALATYA	
20.03.1945	37,11	35,70	6	Ceyhan-ADANA	10
04.08.1951	36,58	35,85	5.7	İskenderun-HATAY	6
14.06.1964	38,13	38,51	6	MALATYA	8
22.05.1971	38,85	40,52	6.7	BİNGÖL	878
22.01.1997	36,25	36	5.5	ANTAKYA	
27.06.1998	36,85	35,55	5.9	Ceyhan- ADANA	
01.05.2003	38,94	40,51	6.4 Mw	Merkez- BİNGÖL	184
14.03.2005	39,41	40,81	5.9 Mw	Karlıova-BİNGÖL	

Table 1.2. Earthquakes that occurred on the EAFZ between 1900 and 2005 (KOERI earthquake catalog

DATE	LATITUDE	LONGITUDE	Mw	LOCATION
08.03.2010	38,87	39,99	6.1	Karakoçan-ELAZIĞ
07.03.2017	37,56	38,40	5.5	Samsat-ADIYAMAN
24.01.2020	38,49	39,12	6.8	Sivrice- ELAZIĞ
14.06.2020	39,34	40,73	5.9	Karlıova-BİNGÖL
04.08.2020	38,13	38,74	5.2	Pütürge-MALATYA
27.12.2020	38,50	39,21	5.6	Kavaktepe-ELAZIĞ
06.02.2023	37,11	37,11	7.8	Pazarcık-KAHRAMANMARAŞ
06.02.2023	38,07	41,15	7.6	Elbistan-KAHRAMANMARAŞ
20.02.2023	36,11	36,08	6.4	Samandağ-HATAY

Table 1.3. Earthquakes that occurred on the EAFZ between 2005 and 2023 (KOERI earthquake catalog)

As evidenced by the list in question, historical and recent earthquakes highlight the significant seismic hazard associated with the EAFZ (Figure 1.6.). These events provide crucial data points for researchers studying future earthquake. Earthquakes in the Hatay region also underscore its vulnerability to seismic activity, given its proximity

to major fault systems like the EAFZ and others in the region. 6 February 2023 Kahramanmaraş earthquakes triggered numerous large and small earthquakes affecting ten surrounding cities in the region. Among these aftershocks, the February 20, 2023 Hatay earthquake stood out as one of the largest and caused significant damage in the Hatay region. Located in the Amik Plain, Hatay is particularly vulnerable to seismic impacts due to its alluvial soil, which can liquefy during earthquakes, leading to structural collapse. This emphasizes the importance of studying the deformation caused by the Hatay earthquakes in the region to better understand fault dynamics and improve seismic hazard mitigation strategies.

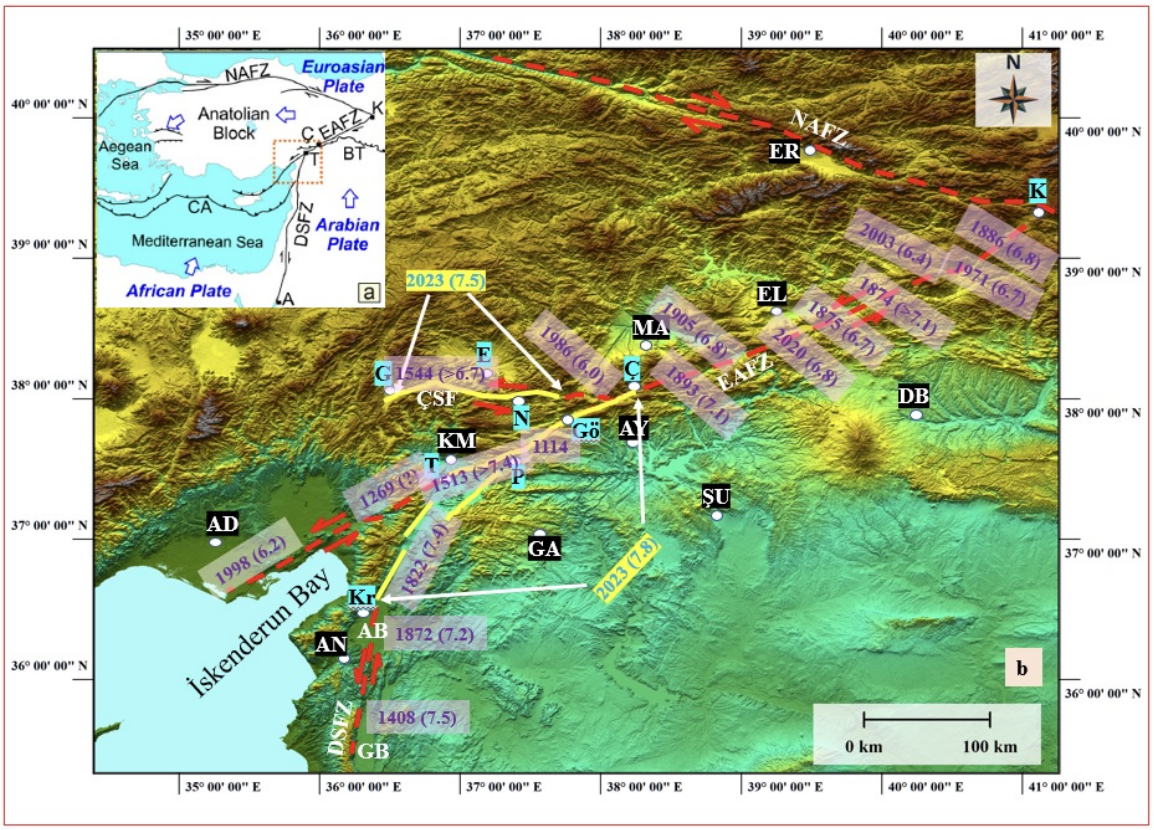

Figure 1.7. This illustration represents the tectonic context and past occurrence of earthquakes in eastern Türkiye, emphasizing several fault lines and notable seismic events. NAFZ : North Anatolian Fault Zone EAFZ : East Anatolian Fault Zone DSFZ : Dead Sea Fault Zone CSF : Central Segment of the Fault C-CAEFZ : Central-East Anatolian Fault Zone ÇSF : Çardak-Sürgü Fault ER : Erzincan K : Karlıova EL : Elazığ MA : Malatya DB : Diyarbakır SU : Şanlıurfa AY : Adıyaman GA : Gaziantep AD : Adana AN : Antakya Ç : Çelikhan GÖ : Gölbaşı P : Pazarcık N : Nurhak E : Elbistan G : Göksun T : Türkoğlu Kr : Kırıkhan AB : Amik Basin GB : Ghab Basin (Alka Tripathy-Lang,2023)

2. METHODOLOGY AND DATA ANALYSIS

In this thesis, the deformation analysis of Hatay earthquake and the inferences obtained as a result of the analysis will be discussed in detail.

The following section will discuss in detail the basic principles of InSAR data analysis, in particular the InSAR Scientific Computing Environment-2 (Rosen et al., 2012) software, ISCE2, along with the practical applications, benefits and inherent limitations of InSAR.

2.1. SAR Interferometry

Synthetic Aperture Radar (SAR) is a remote sensing method based on radar technology that enables the generation of high-resolution images of the Earth's surface. This is achieved by transmitting electromagnetic wave (microwave) signals towards the Earth's surface, which are then reflected back to the radar antenna, allowing the backscattered signals (echoes) to be recorded in both amplitude and phase (Figure 2.1). In the SAR method, a moving antenna mounted on a satellite or aircraft is used and the movement of the radar antenna provides a very large antenna aperture. This aperture is called as synthetic aperture and increases the resolution of the radar image. The amplitude and phase information obtained from the backscattered signal provides us with different insights into the Earth's surface, contingent on the distance and characteristics of the reflected objects. For example, phase values are essential for calculating deformation In the SAR interferometry (InSAR), while amplitude values provide information about the target geometry, roughness, dielectric constant and wetness.

One of the benefits of employing active data sources in remote sensing applications, such as SAR data, is the capacity to gather data in all weather conditions, including during the day and night, as well as on cloudy days. Additionally, the capac-

ity to generate deformation maps of expansive areas represents a notable advantage, due to the extensive area coverage afforded by the technology. Furthermore, the capacity to attain exceedingly high spatial resolutions is a significant advantage, with the potential to reach a few meters or less, based on the frequency utilized.

The common frequency bands used in the SAR method are given in Table 2.1. It has a wide range from high frequency of 8-12 GHz (X band) to low frequency of 1-2 GHz (L band). High frequencies represent high-resolution SAR images. Therefore, short wavelength data (3.8-2.4 cm) are usually used for urban monitoring, while longer wavelengths $> 7.5cm$ are preferred for global mapping and change detection. Even longer wavelengths are predominantly utilized for geophysical monitoring and vegetation mapping, largely due to their high penetration ability (Table 2.1). In this thesis, the C-band SAR data images were utilized for the deformation analysis in Hatay region. The SAR instrument operates in one of four modes; Stripmap (SM), Interferometric Wide Swath (IW), Extra Wide Swath (EW), Wave (WV).

The goal of Interferometric Synthetic Aperture Radar (InSAR) techniques is to combine two or more SAR images over the same region to reveal surface motions. The main purpose of these combinations is to obtain a new image by calculating the pixel differences from images taken at the same place at different times. This new image is used as an interferogram.

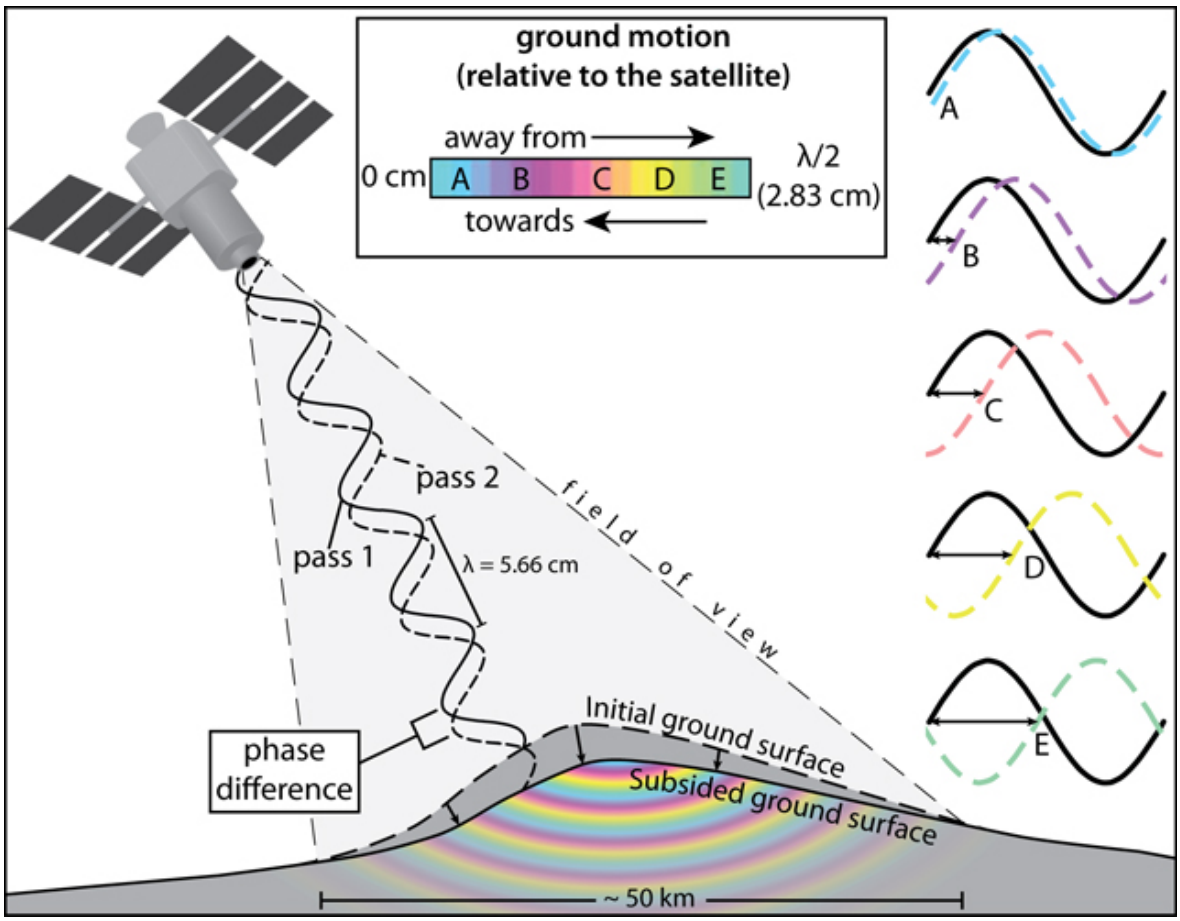

Figure 2.1. This diagram depicts the principle of using satellite-based Interferometric Synthetic Aperture Radar (InSAR) to measure ground movement. The demonstration illustrates the capability of satellites to identify alterations in the Earth's surface over a period of time by analyzing two radar pictures captured at distinct moments. (www..volcano.si.edu)

The Figure 2.1 shows the principle of using satellite-based InSAR to measure ground movement. The demonstration illustrates the capability of satellites to detect changes in the Earth's surface over a period of time by analyzing two radar pictures captured at distinct moments. Pass 1 and Pass 2 represent two instances in which the satellite passes over the same region with a time interval between them. The satellite transmits radar waves towards the Earth's surface and captures the reflected signals. The differences in the phase of the radar waves between the two passes give the phase difference for subsidence in the example case and utilized for quantifying

ground movement. The wavelength, the distance between consecutive crests of the radar wave, is 5.66 cm in this instance. The ground motion is classified into several segments (A, B, C, D, E) according to the direction and magnitude of the displacement relative to the satellite. The colors in Figure 2.1 are categorized as (i) A (colored blue) is not moving; (ii) B (purple) slight deviation from the satellite's position; (iii) C (red) moderate movement; (iv) D (yellow) substantial movement from its original position; (v) E (green) maximum deflection toward the satellite.

Band	**Frequency**	**Wavelength**	**Typical Application**
X	8–12 GHz	3.8–2.4 cm	High resolution SAR (urban monitoring; ice and snow, little penetration into vegetation cover; fast coherence decay in vegetated areas)
C	4–8 GHz	7.5–3.8 cm	SAR Workhorse (global mapping; change detection; monitoring of areas with low to moderate penetration; higher coherence); ice, ocean maritime navigation
S	2–4 GHz	15–7.5 cm	Little but increasing use for SAR-based Earth observation; agriculture monitoring (NISAR will carry an S-band channel; expands C-band applications to higher vegetation density)
L	1–2 GHz	30–15 cm	Medium resolution SAR (geophysical monitoring; biomass and vegetation mapping; high penetration, InSAR)

Table 2.1. SAR frequency bands

The InSAR technique combines two or more SAR images which have phase information over the same region to reveal surface motions with high precision. The main purpose of these combinations is to obtain a new image by calculating the phase differences in each pixel from images taken at the same place at different times. This

new image is called as an interferogram (Figure 2.2). The wave traveling back and forth between the satellite and the surface is called oscillation. The phase of the radar signal gives the number of oscillation cycles. Adding random path lengths confuses the phase of the echo. An interferogram is used to remove this confusion.

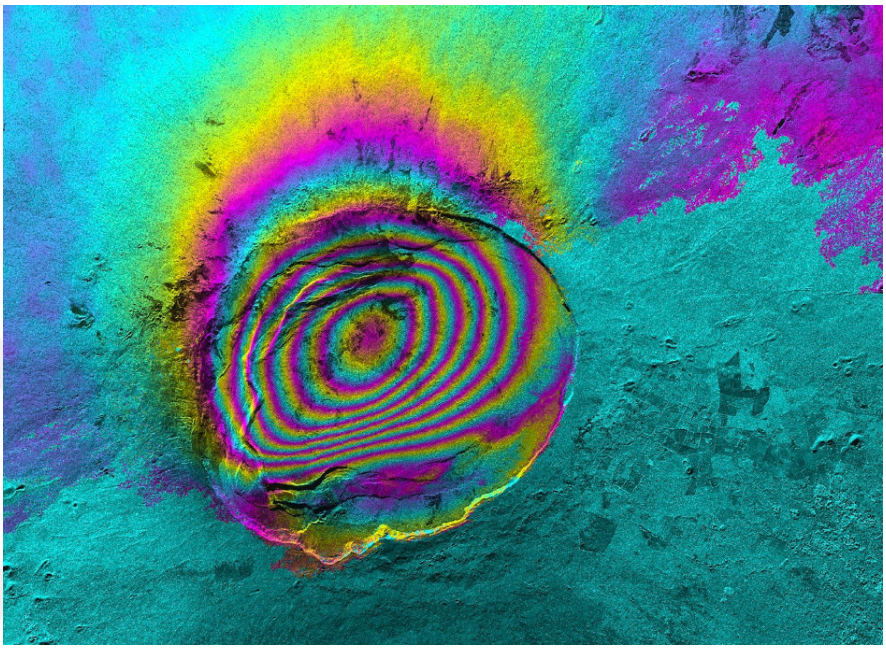

Figure 2.2. This figure depicts the InSAR image. The concentric circles (fringes) and variations in the image signify the magnitude and pattern of surface displacement over a period of time. (Figure by NASA)

Combining two separate radar images capturing the same area reveals changes in the area by radar waves backscattered from ground features with a different signal phase, manifested in colored interference patterns known as fringes on the combined image.

The transmitted wave from the radar device travels to ground scatterers and is then reflected back to the device. This process requires a round trip. The transmission and reception of radiation is subject to delays due to scatterers located at different distances, known as slant ranges. These delays, can be in the time interval between two SAR observations and are manifested as phase changes, φ, due to the sinusoidal nature of the signal. The phase shift, φ, is proportional to the two-way travel distance

(2R) of the radiation divided by its wavelength, λ. The formula to be used to observe this change is given in Equation 2.1.

$$\Delta\phi_d = \frac{4\pi}{\lambda} d \tag{2.1}$$

The interferometric phase shift can be decomposed into two different components; these are a phase change proportional to the height difference q between the point targets and a horizontal reference plane, and a phase change proportional to the displacement along the slant range of the point targets (Equation 2.2).

$$\Delta\phi = -\frac{4\pi}{\lambda} \frac{B_n q}{R \sin\theta} + \frac{4\pi}{\lambda} d \tag{2.2}$$

where π is the radiation incidence angle with respect to the reference. The first part of the Equation 2.2 represents the variation due to the height (altitude) difference and the second part represents due to the slant range displacement.

If a digital elevation model (DEM) is available, the elevation contribution can be subtracted from the interferometric phase (forming what is called a differential interferogram) and the terrain motion component can be measured. Assuming a perpendicular baseline of 150 m with $\lambda = 5.6$ cm (a fairly common value), the following expression holds (ERS case is given): (Equition 2.3)

$$\Delta\phi = -\frac{q}{10} + 225d \tag{2.3}$$

2.1.1. Steps for InSAR analysis using TopsApp in ISCE2

InSAR, is a very effective method of remote sensing that is utilized for the precise measurement of ground deformation and alterations in topography. ISCE2, also known as InSAR Scientific Computing Environment, is a software framework specifically developed for the processing of SAR data. Within ISCE2, there is a specialist application

called TopsApp, which is created specifically for processing Terrain Observation with Progressive Scans (TOPS) SAR data obtained from satellites like Sentinel-1. In accordance with the instructions set forth in the ISCE2 manual, the installation process entailed the creation of a Python environment and the installation of requisite dependencies. For the purpose of data analysis, C-band Sentinel-1 SLC data for both ascending and descending orbits were obtained from the NASA Alaska Satellite Facility website. The data set comprised both primary acquisitions (obtained prior to the earthquake) and secondary acquisitions (obtained subsequent to the earthquake). After downlading data, a directory was created for the project, and the downloaded SAR data was sorted into folders according to the dates of their respective collections. A configuration file, entitled "topsApp.xml," has been generated within the directory of our project. This file includes the requisite parameters and paths for the processing procedure. Prior to processing the InSAR data, a digital elevation model (DEM) sourced from the Shuttle Radar Topographic Mission (SRTM) at a resolution of 3 arc seconds (90 m) was obtained. This DEM is used to flatten the data in the InSAR process, which involved the removal of the topographic phase component from interferograms. Additionally, precise orbit data were downloaded. In the co-registration step, the primary and secondary SAR images from disparate acquisition times are aligned with exact precision, accounting for any geometric distortions or misalignments to a subpixel level. Later, by taking the complex conjugate multiplication of two co-registered SAR images, the interferogram is computed in order to examine the phase discrepancy between the SAR images. This yields an interferometric phase image, wherein each pixel signifies the phase discrepancy between the two acquisitions. The interogram are first obtained for the bursts and then they are merged into a single uninterrupted interferogram. A noise reduction filter has been implemented to enhance the quality of the phase in the next step. Following that, the process involves converting phase values that were initially wrapped in the range 0 to 2 π into continuous phase values. This is accomplished using an unwrapping algorithm such as Snaphu. The final results consist of geocoded interferograms, unwrapped phase images, and additional supporting data. These items are essential for the analysis of ground deformation and topography alterations.

2.2. DATA Set

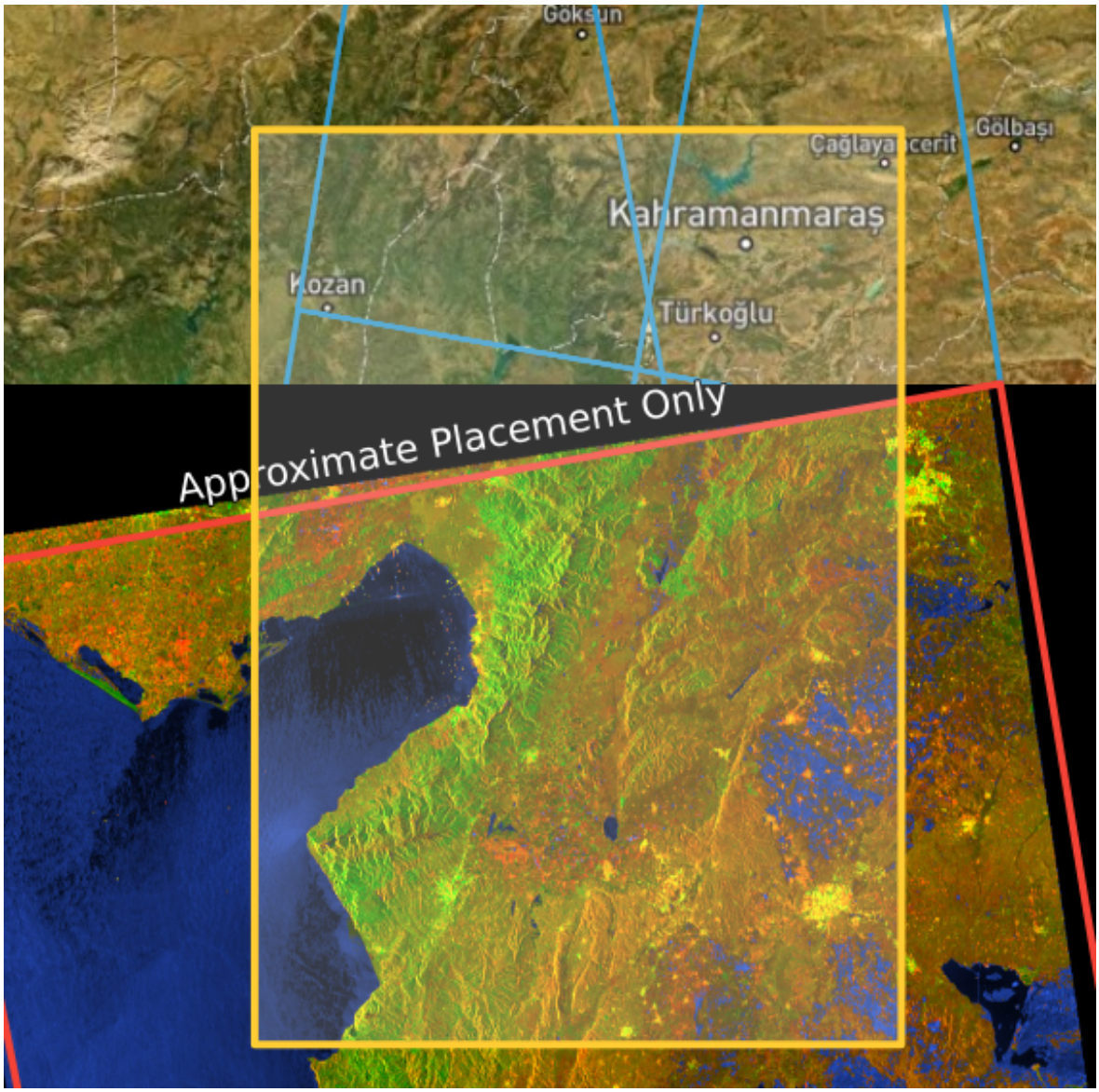

Figure 2.3. This figure shows the study area.

In this thesis, in order to obtain better results on deformation; ascending and descending data from before and after the February 20, 2023 Hatay earthquake were used. Therefore, the following images were selected as the data.

For Ascending data; Path: 14, Frame: 114 images were selected for the period 9 February 2023 – 21 February 2023. On the other hand, for descending data; Path: 21, Frame: 471 images were selected for the period 10 February 2023 – 22 February 2023.

2.3. Co-Seismic Deformation

InSAR, is a very accurate remote sensing method employed to quantify ground displacement caused during co-seismic or post-seismic deformation. Co-seismic deformation is the term used to describe the movement of the Earth's surface that happens during an earthquake. The use of InSAR is especially advantageous for evaluating this type of deformation since it may offer uninterrupted, high-resolution observations across extensive regions.

InSAR utilizes radar pictures obtained from satellites both prior to and following an earthquake. The purpose of these photos is to create interferograms, which visually depict the variation in phase between the radar signals before and after the occurrence. The phase difference is directly proportional to the magnitude of ground movement.

To generate an interferogram, the radar signals obtained from two or more acquisitions are compared. An interferogram is a visual representation of the Earth's surface displacement, depicted as a sequence of fringes or contour lines. Each fringe corresponds to a precise measure of displacement, usually in the range of millimeters.

Co-seismic deformation is determined by extracting the displacement that occurred specifically during the earthquake from the interferograms. This entails: The process of distinguishing the co-seismic signal involves isolating the deformation that occurs during an earthquake from other signals, such as post-seismic deformation or long-term trends. Compensating for Atmospheric Effects: Radar signals can be influenced by atmospheric circumstances, necessitating adjustments to guarantee the accuracy of deformation readings. Geocoding and calibration involve the conversion of interferograms into real-world coordinates and the alignment of observations with ground truth data.

The resultant displacement maps offer valuable information about the spatial arrangement and extent of the ground displacement. High-resolution maps facilitate the

identification of the fault rupture and the regions that are most impacted by the earthquake. The co-seismic deformation that is seen is analyzed in relation to theoretical models of fault rupture in order to gain insight into the mechanics of the earthquake and verify the accuracy of the models.

InSAR method is widely used in analysis of fault parameters and damage assesment in seismological researches. Has the capability to unveil the precise dimensions and properties of the fault rupture, encompassing its length, width, and distribution of displacement. This information is vital for comprehending the impact of the earthquake and for assessing seismic hazards. InSAR aids in evaluating the magnitude of harm to infrastructure and communities by creating maps of surface deformation. This information is crucial for the purposes of disaster response and recovery endeavors. InSAR data enhances our comprehension of earthquake mechanisms, namely the connection between fault displacement and surface distortion.

There are some challenges in InSAR data analysis. The resolution of InSAR data can be influenced by factors such as satellite orbit and radar system parameters. High-resolution data is crucial for in-depth research but may necessitate the use of sophisticated processing techniques. Fluctuations in atmospheric conditions might cause inaccuracies in the interferograms. Methods such as adjusting for air conditions and utilizing several radar scans can help reduce the impact of these phenomena. InSAR analysis relies on the presence of radar images taken before and after the incident. Temporal gaps can restrict the precision of co-seismic deformation estimates.

2.4. Interferograms Generation

For the purpose of data analysis, C-band Sentinel-1 SLC data for both ascending and descending orbits were obtained from the NASA Alaska Satellite Facility website. The data set comprised both primary acquisitions (obtained prior to the earthquake) and secondary acquisitions (obtained subsequent to the earthquake).

Images to generate an interferogram, several images of the similar region are captured at various time intervals, from essentially indistinguishable spatial locations.In the context of data analysis, the SAR images captured prior to the Hatay earthquake were designated as primary data, while those obtained subsequent to the seismic event were classified as secondary data.

The phase information from the radar signals in the primary and secondary images were compared. An interferogram was formed by the phase difference between these images, which is represented as fringes. Figures 2.4 and 2.6. indicate the wrapped interferograms generated from the ascending and descending data, respectively.

The interferogram displays phase disparities that are confined within the range of - π to + π . Phase unwrapping is the procedure of transforming wrapped phase variables into uninterrupted displacement values. Figures 2.5 and 2.7. represent the unwrapped interferograms generated from the ascending and descending data, respectively. Accurate measurements of ground displacement are acquired by studying the unwrapped phase. These measures can be indicative of subsidence, uplift, or horizontal displacement of the ground surface as it is observed in Hatay region.

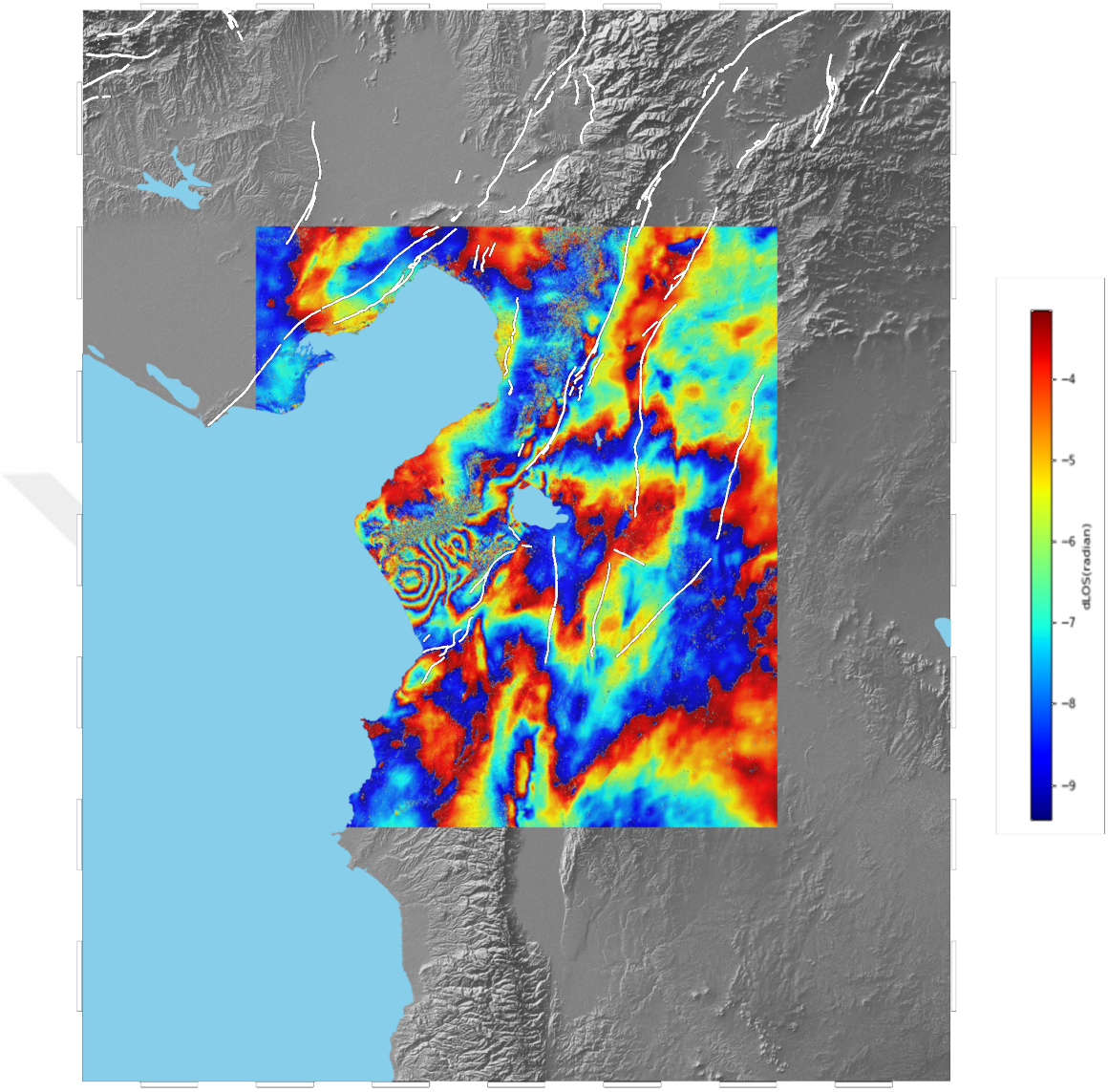

Figure 2.4. Ascending wrapped interferogram obtained from the analysis of frame 114 SAR data to investigate the deformation due to the Hatay earthquake.

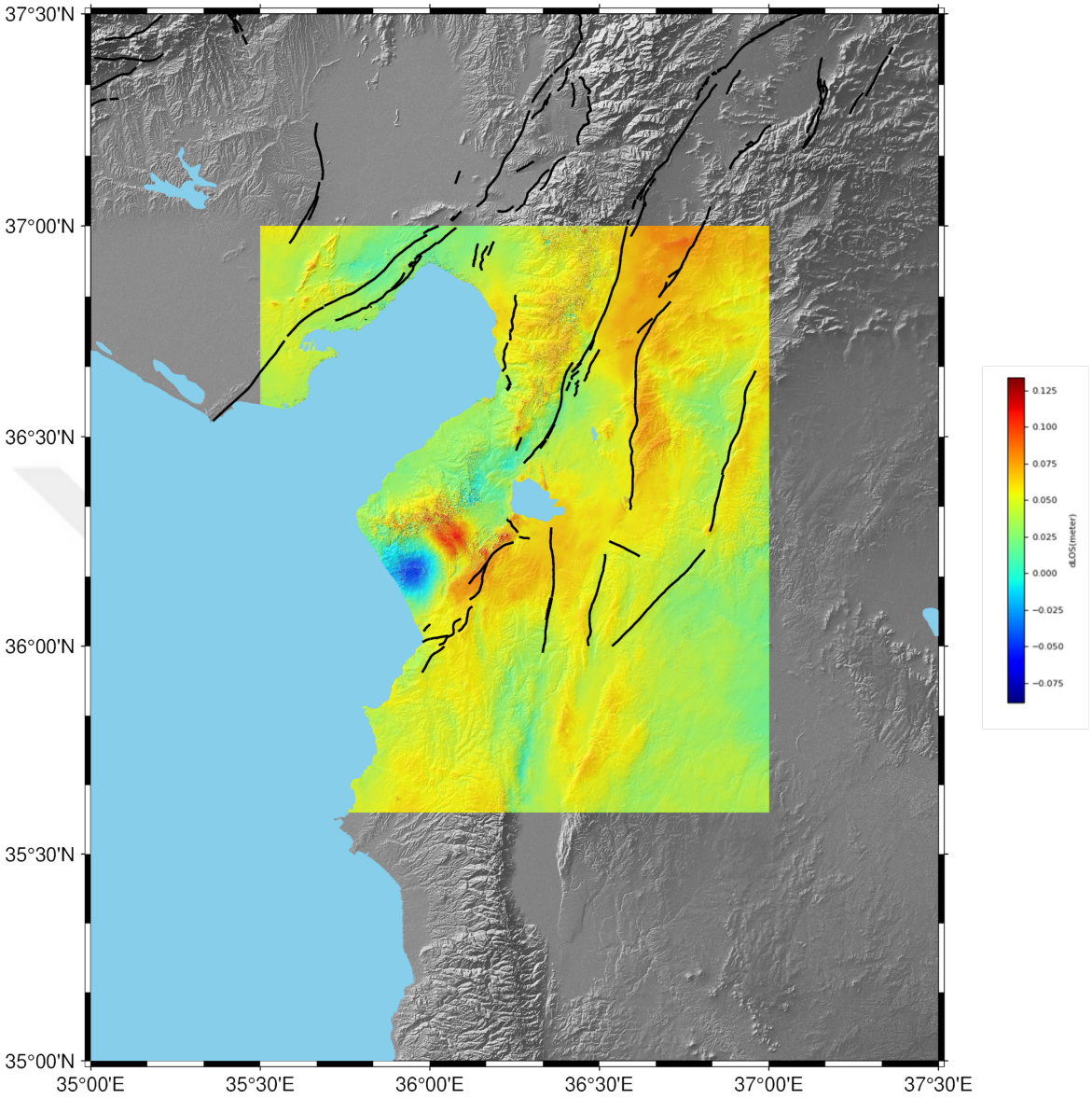

Figure 2.5. Ascending unwrapped interferogram obtained from the analysis of frame 114 SAR data to investigate the deformation due to the Hatay earthquake.

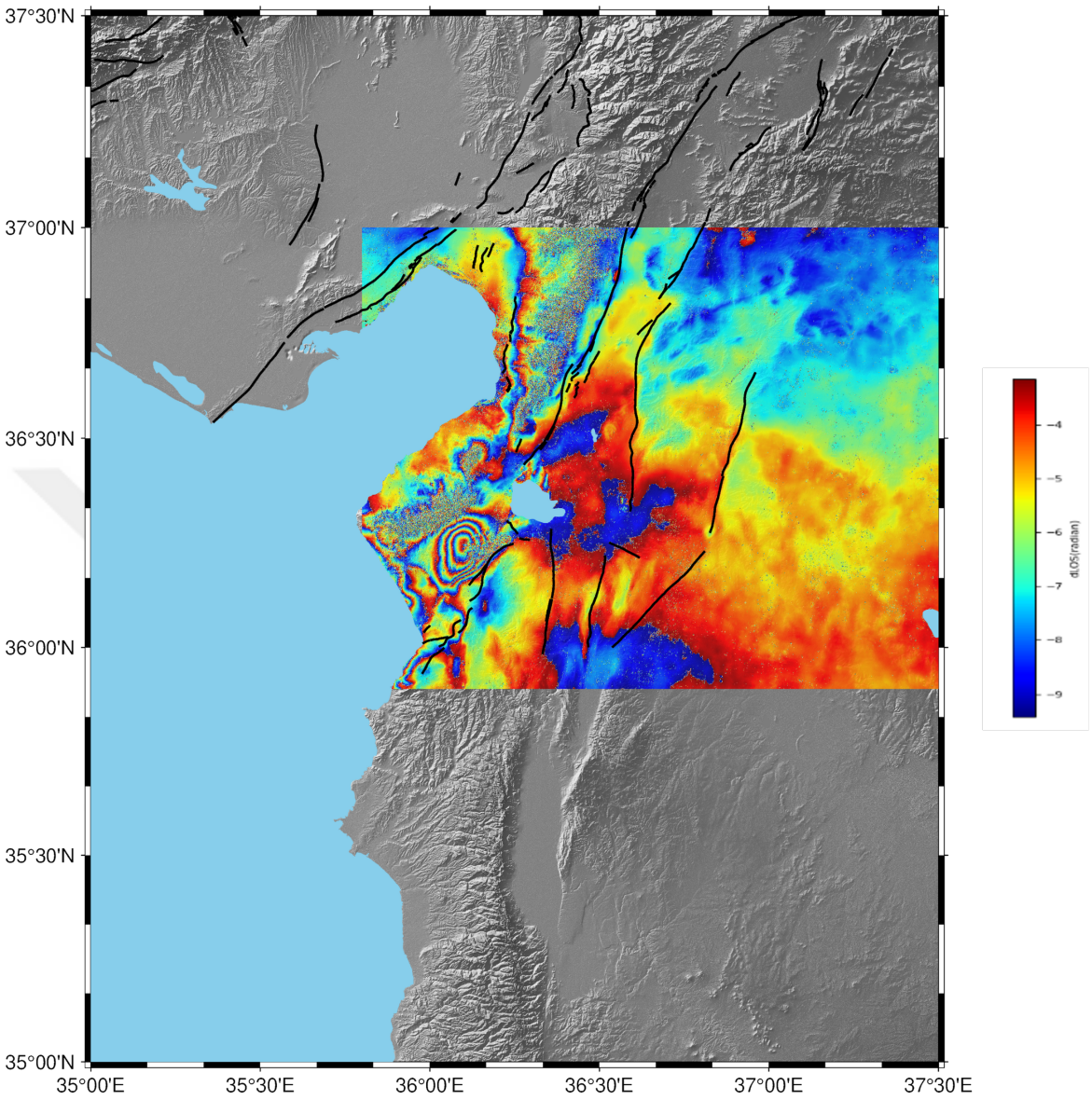

Figure 2.6. Descending wrapped interferogram obtained from the analysis of frame 471 SAR data to investigate the deformation due to the Hatay earthquake.

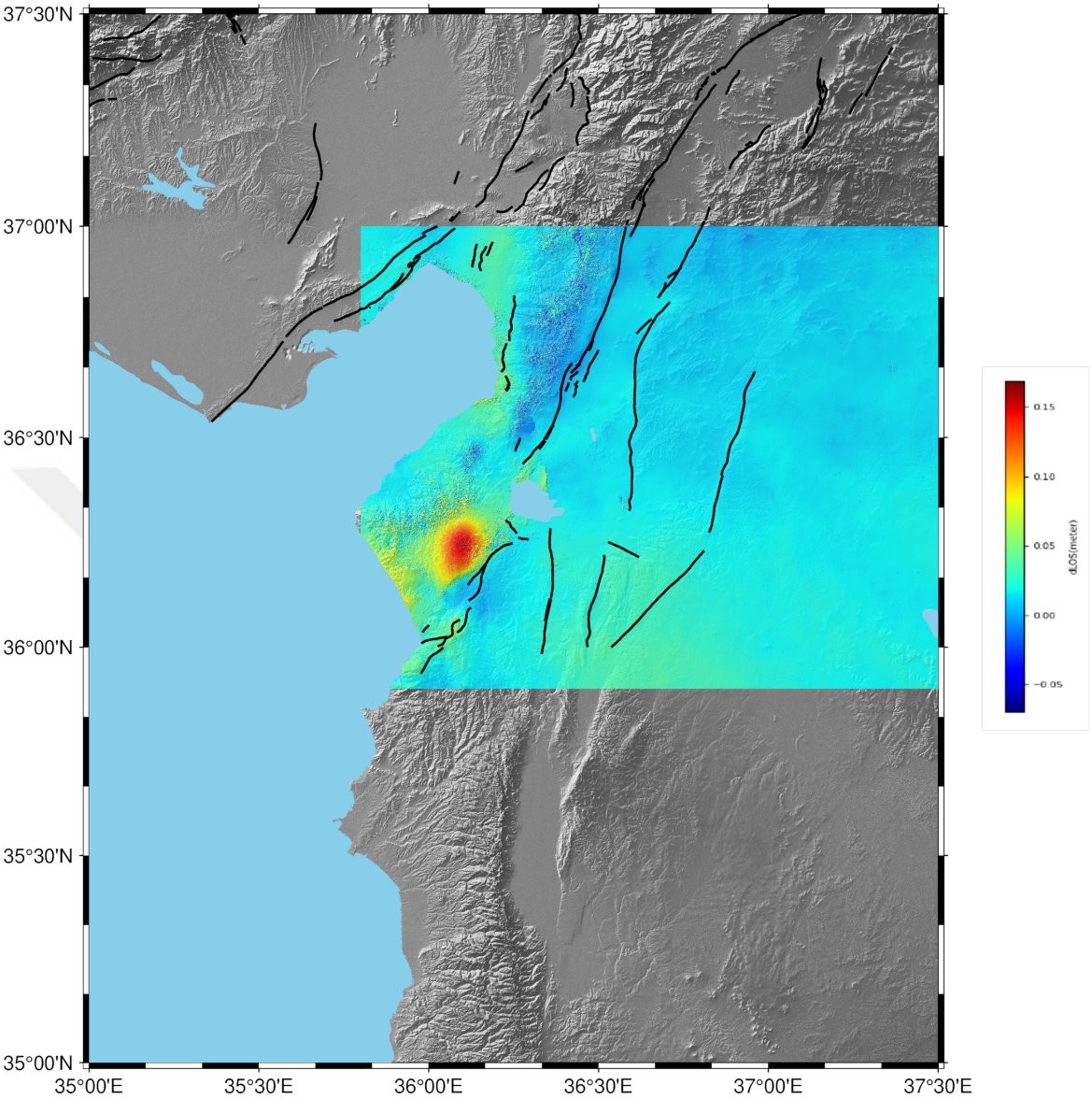

Figure 2.7. Descending unwrapped interferogram obtained from the analysis of frame 471 SAR data to investigate the deformation due to the Hatay earthquake.

2.5. Tropospheric Correction

The atmospheric effects on the paths of each oscillation may differ depending on the time interval between the acquisition of two interferometric SAR images. The effects, in particular, different atmospheric humidity, temperature, pressure, etc. between two shots, will have a visible consequence on the interferometric phase.This effect is generally limited to the 2 π peak-to-peak interferometric range. With uniform spatial

variability (from a few hundred meters to a few kilometers) there can be phase change across the image. The effect of such a contribution affects both altitude and terrain deformation measurements.

In this study, Sentinel-1 SAR data was used to create 2023 InSAR interferograms. The two ESA Sentinel-1 satellites (S1A and S1B) have a 6-day repeat period and carry a 56-day C-band synthetic aperture radar. It has mm wavelength and four operating modes. 5 × 20 m resolution footage was used in Interferometric Wide (IW) mode. Processing of InSAR data was done using the ISCE application. Tropospheric corrections were made using Jupyter notebook with the data generated from ISCE. Tropospheric correction took place before the interferogram was opened. This was done to minimize phase ambiguities and increase the reliability of the interferogram unpacking process, where coherence is low due to vegetation and rough topography, leading to geometric decoration.

Tropospheric corrections are given below :

2.5.1. Converting zenith tropopsheric delay to slant phase delay

Next, we will project the zenith delay into the radar slant (radar look direction) by using a simple cosine mapping function of the incidence angle, and at the same time apply the scaling to convert from pseudo-range to phase

$$\Phi_{\text{slant}} = \frac{-4\pi}{\lambda \cdot \cos(\theta)} \cdot d_{\text{zenith}} \tag{2.4}$$

2.5.2. InSAR Tropospheric Phase Delay (slant)

Now that we have a tropospheric phase delay estimated for both SAR acquisitions, we can compute the differential delay. Note it is important to apply the same convention as you did when making the interferogram. Below we include the **differential delay** function which takes a reference and secondary APS files as input as well as an output name.

$$\Delta\Phi_{\text{slant}} = \Phi_{\text{slant}}^{\text{reference}} - \Phi_{\text{slant}}^{\text{secondary}} \tag{2.5}$$

Hatay Earthquake 20 February, 2023 Ascending Data

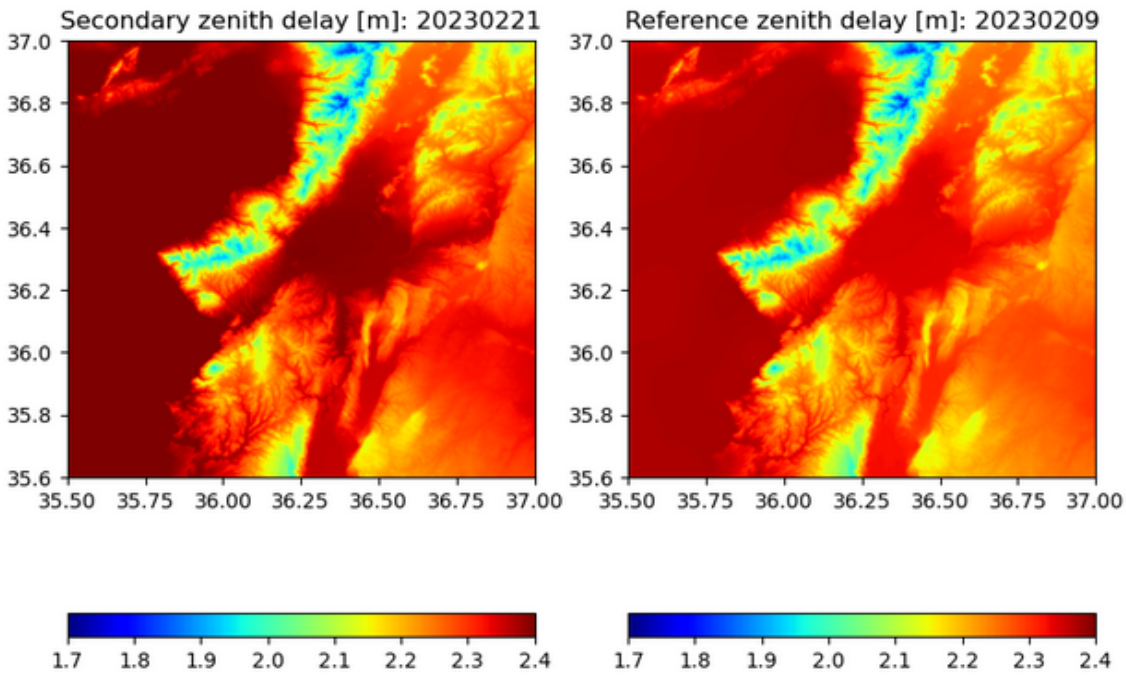

Figure 2.8. The Ascending data the zenith delays for two distinct dates: February 21, 2023 (Secondary) and February 9, 2023 (Reference).

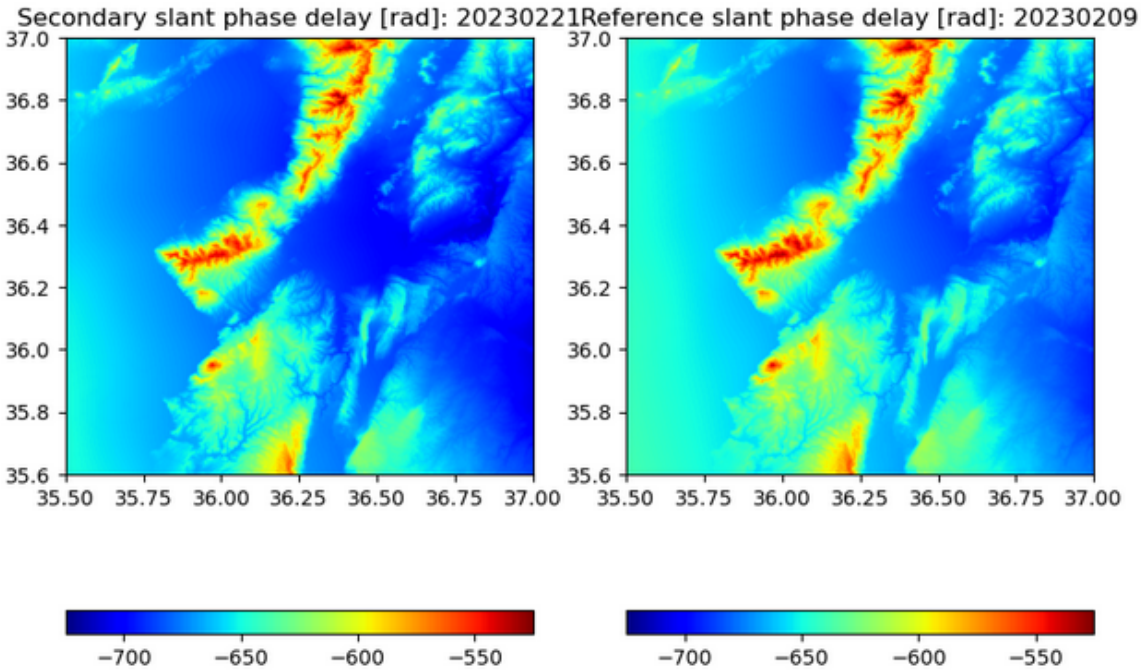

Figure 2.9. Reference and secondary slant phase delays. The labels indicate the dates of the radar acquisitions used in the InSAR analysis. The secondary image was acquired on February 21, 2023, and the reference image on February 9, 2023.

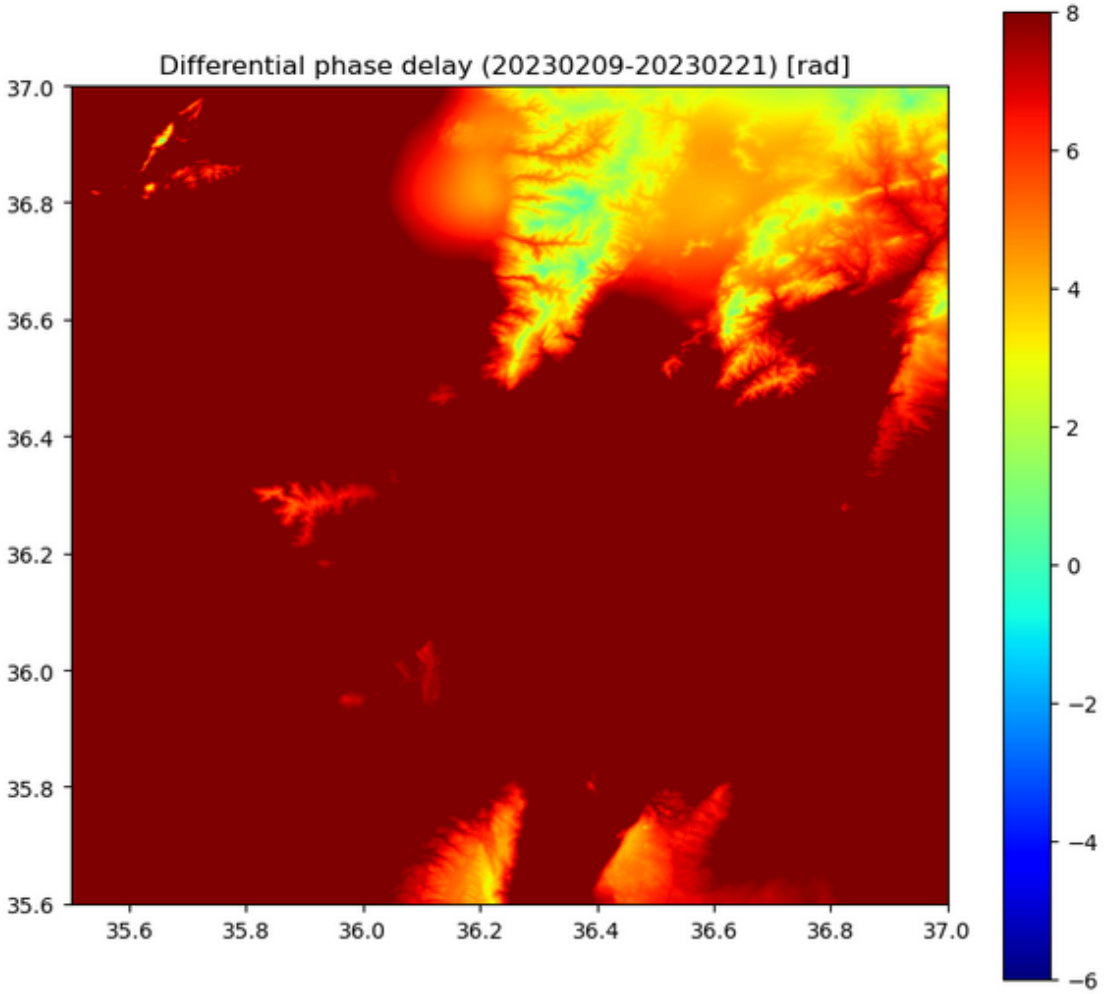

Figure 2.10. The provided image is a differential interferogram showing the "Differential phase delay (20230209-20230221) [rad]." This map represents the phase difference between radar images acquired on February 9, 2023, and February 21, 2023.

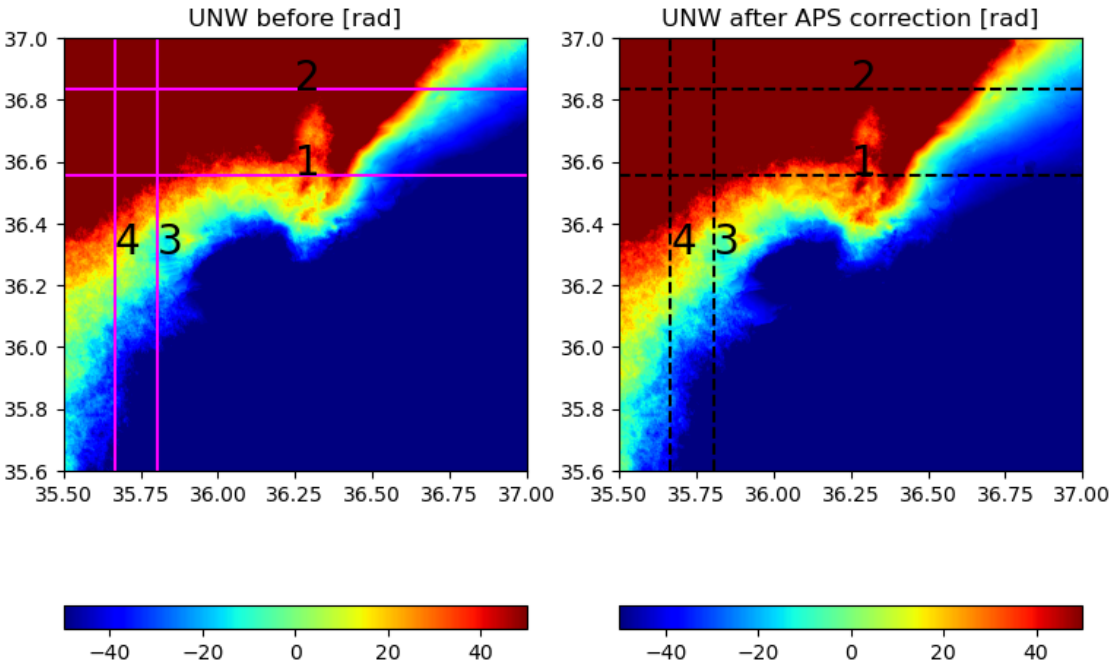

Figure 2.11. The unwrapped interferogram is presented both before and after application of the APS correction to the ascending data.

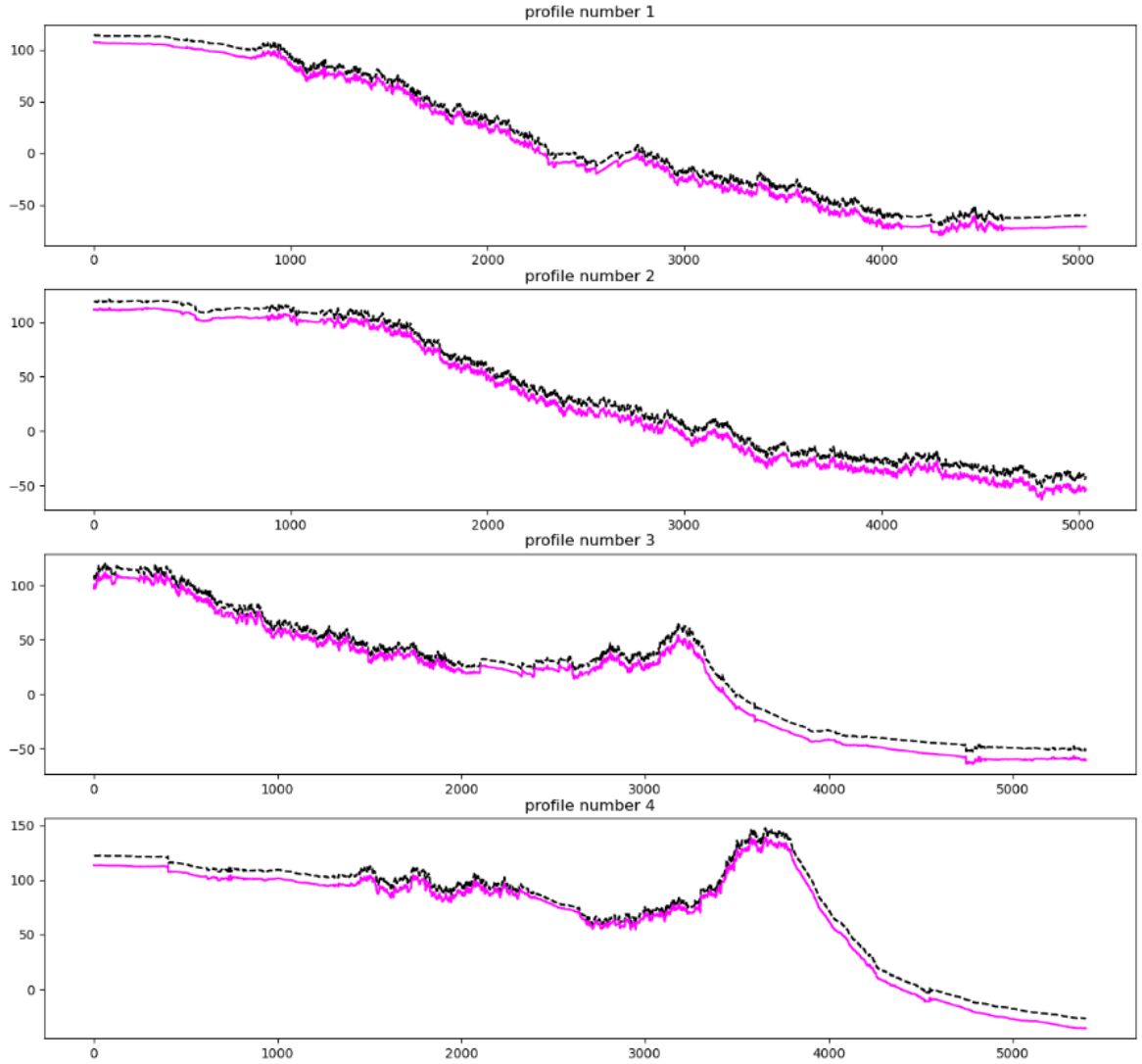

Figure 2.12. The APS correction cross-sections taken along profiles 1 to 4 shown in Figure 2.11.

Profile Number 1: The uncorrected phase values are represented by the magenta solid line. The black dashed line displays the phase values following APS correction. The revised profile nearly mirrors the original profile, but with a notable enhancement in minimizing phase fluctuations.

Profile Number 2: Like Profile 1, the adjusted phase values exhibit a strong resemblance to the unadjusted values, but with a decrease in volatility.

Profile Number 3: The revised profile exhibits more prominent enhancements, especially in areas with greater phase fluctuations. The general pattern is more effectively maintained after the modification.

Profile Number 4: The profile exhibits a notable phase fluctuation towards the conclusion, which is more well handled in the revised data. The rectified profile line has a more even and polished appearance in contrast to the unrectified one, signifying the effective correction of APS.

Hatay Earthquake 20 February, 2023 Descending Data

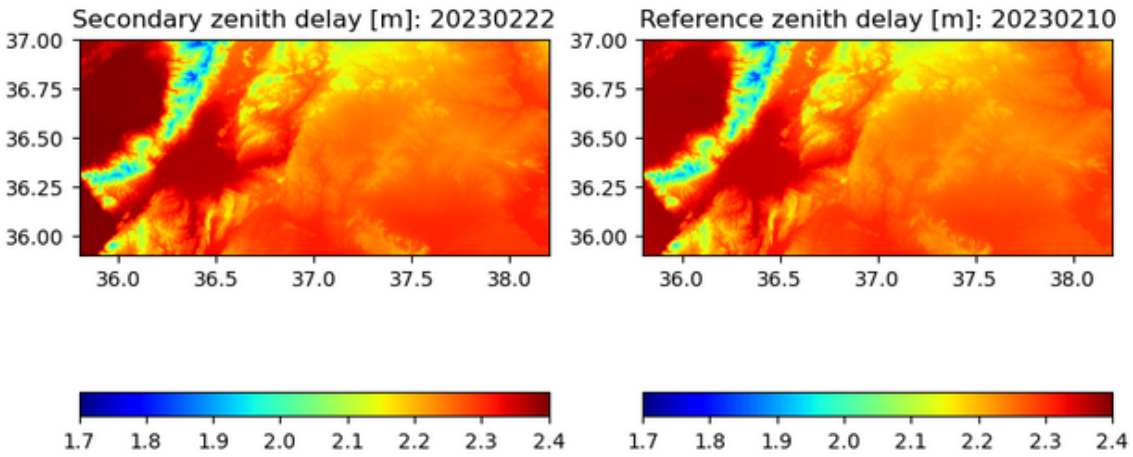

Figure 2.13. The provided image consists of two maps showing "Secondary zenith delay [m]: 20230222" and "Reference zenith delay [m]: 20230210."

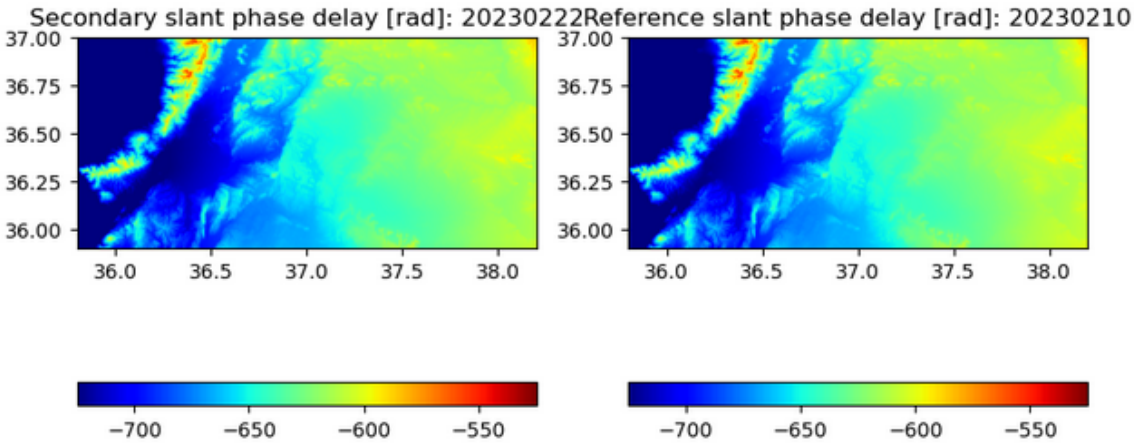

Figure 2.14. Reference and secondary slant phase delays for descending data. The labels indicate the dates of the radar acquisitions used in the InSAR analysis. The secondary image was acquired on February 22, 2023, and the reference image on February 10, 2023.

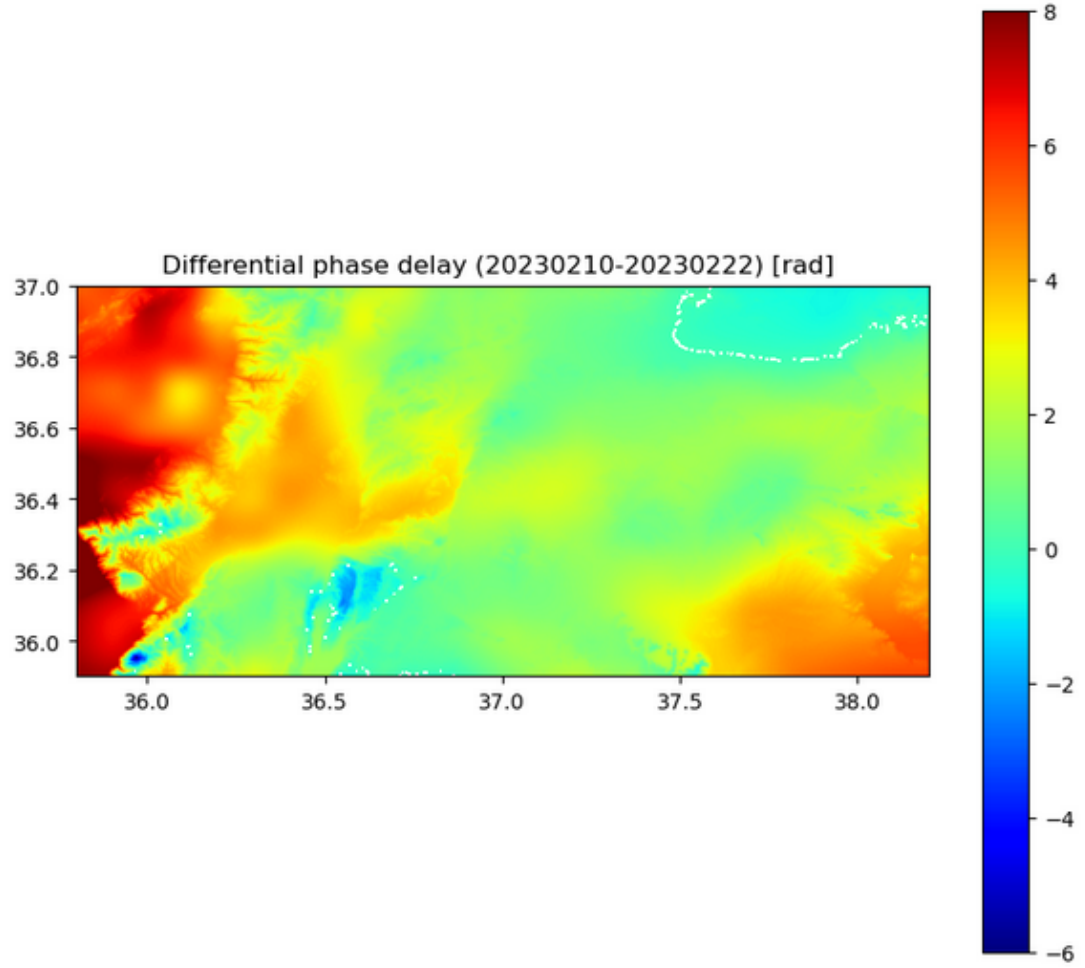

Figure 2.15. Differential phase delay between radar images taken on February 10, 2023 and February 22, 2023 (descending orbit).

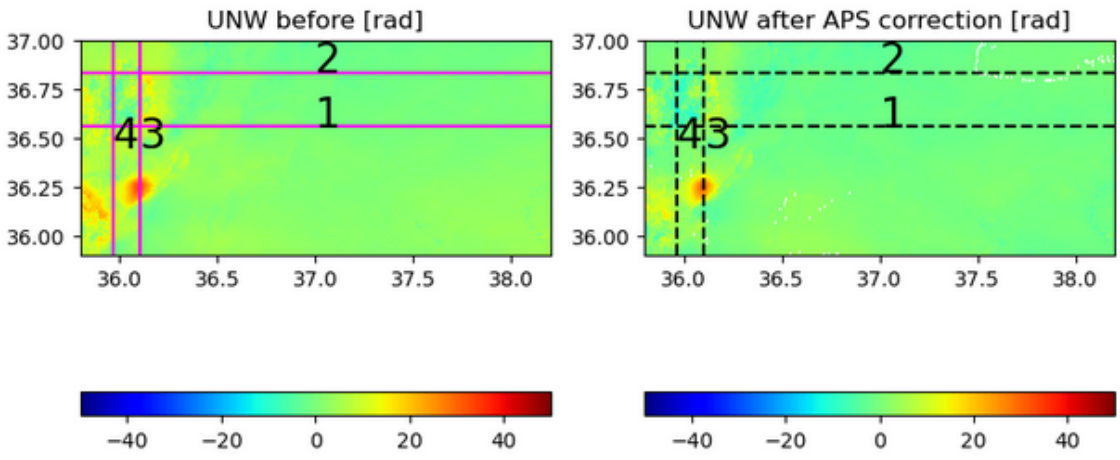

Figure 2.16. The unwrapped interferogram is presented both before and after application of the APS correction to the descending data.

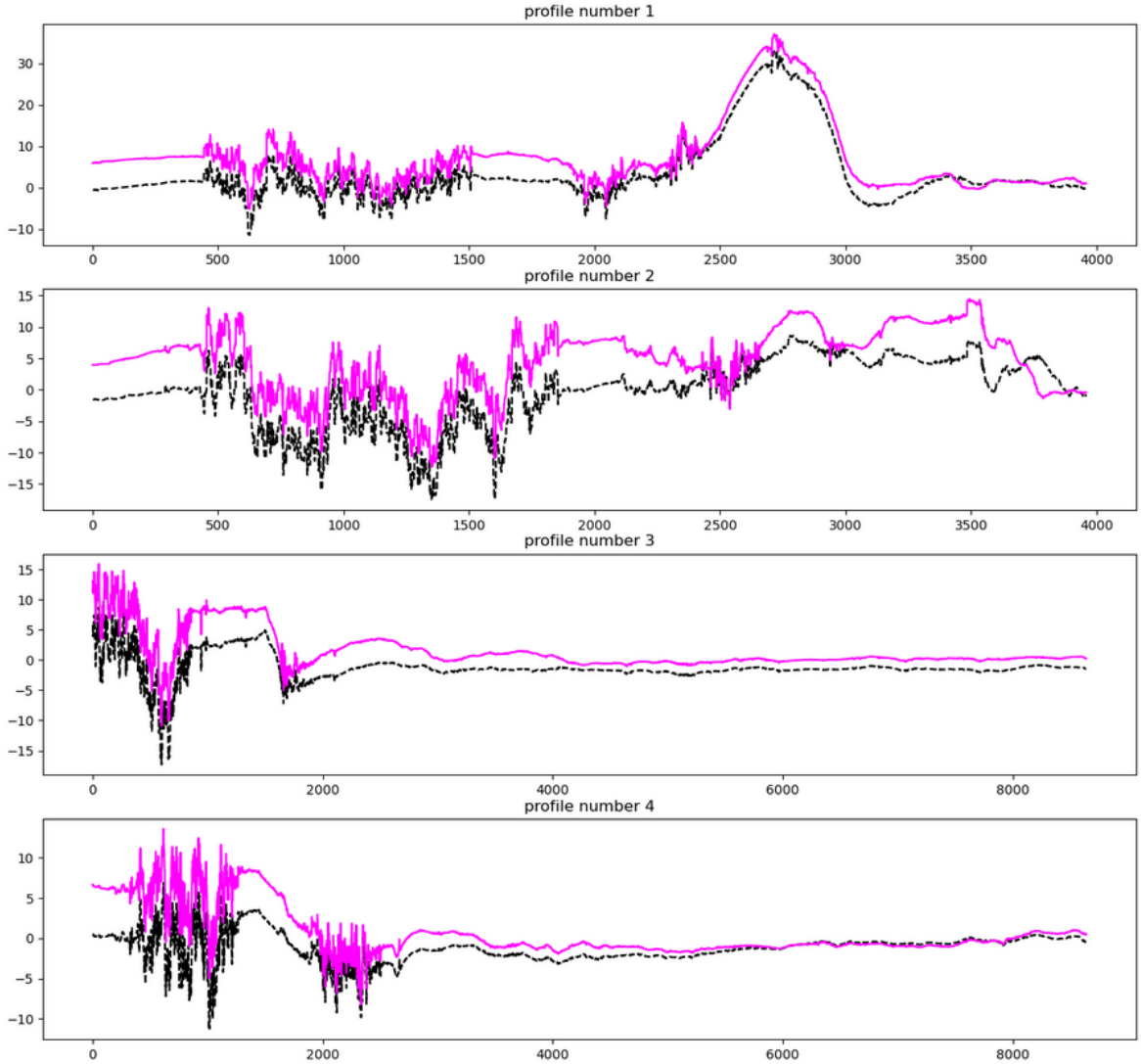

Figure 2.17. The APS correction cross-sections taken along profiles 1 to 4 shown in Figure 2.16.

Profile 1: The pink solid line and the black dashed line depict the data before and after APS correction. The prominent spike at 2500 units on the x-axis shows a substantial increase or decrease in ground elevation.

Profile Number 2: As in Profile 1, this profile also displays displacement along a distinct trajectory. Variations in the pink line relative to the black dashed line suggest alterations in deformation, maybe caused by diverse ground conditions or interactions between faults. The profile exhibits substantial noise, which can be ascribed to air

disturbances or local geological changes.

Profile Number 3: This profile exhibits a comparatively steady baseline (shown by the black dashed line) with less fluctuations. The pink line exhibits a less prominent although still discernible distortion.

Profile Number 4: This profile has an extended range, reaching up to 8000 units along the x-axis. The pink line closely adheres to the black dashed line, demonstrating less distortion over this extended distance compared to the other profiles.

2.6. HypoDD

The HypoDD algorithm, also known as the "Hypocenter Double-Difference" algorithm, is a commonly employed technique for the relocation of earthquakes. It enhances the accuracy of determining the hypocenter of an earthquake and aftershocks by utilizing double-difference (DD) technique, which refer to the variations in travel times between pairs of earthquakes that are detected at the seismic stations. The process involves reducing the discrepancies of the double-difference equations by utilizing both absolute and differential trip durations to improve the accuracy of the locations.

The research area's seismic hypocenters were relocated with more accuracy by applying HypoDD in the thesis. Figure 2.18. shows t relocated aftershock distribution of Kahramanmaraş earthquakes (Özener et al., EGU2023) processed with HypoDD technique.

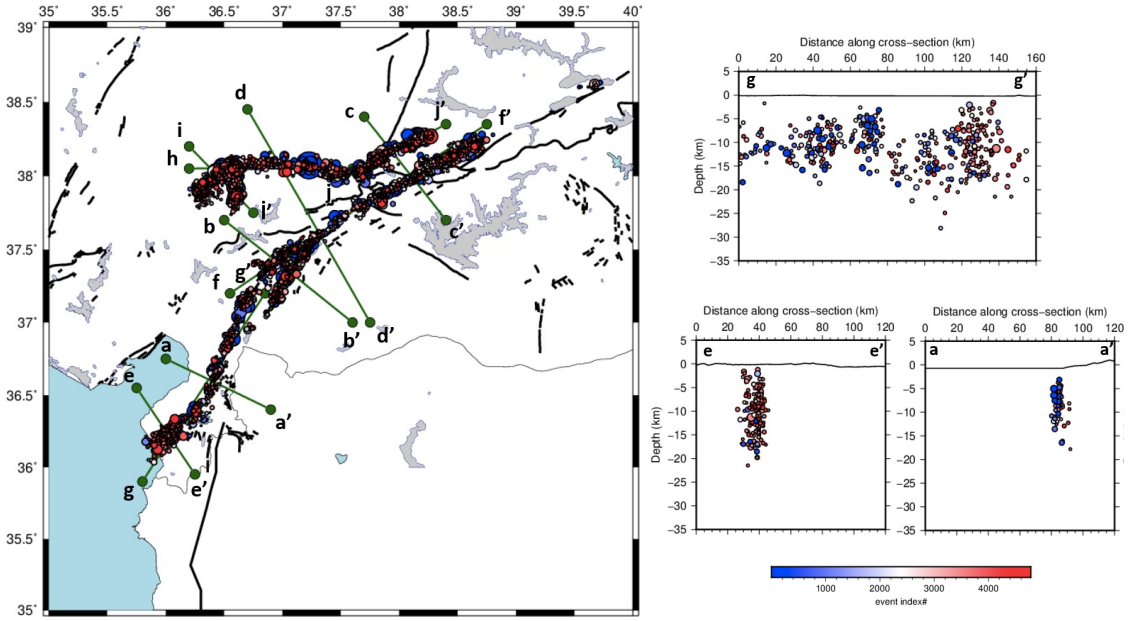

Figure 2.18. Aftershock distribution of Kahramanmaraş earthquakes (Özener et al., EGU2023) processed with HypoDD technique (Waldhauser and Elsworth, 2000). Letters on the map indicate the locations of the cross sections. Depth sections of the relocated earthquake distribution along the profiles in Hatay region are also given.

The utilization of both P-wave and S-wave travel periods was employed to augment the accuracy of the relocations. The repositioned hypocenters yielded a more distinct depiction of the fault structures. The enhanced locations facilitated the comprehension of the seismotectonic characteristics of the area. HypoDD greatly enhanced the precision of earthquake locations, resulting in more accurate understanding of fault geometry and seismicity patterns. The earthquake database that was transferred provided more intricate seismicity patterns, which are crucial for assessing seismic hazards. Enhanced knowledge of fault structures and their dynamics during seismic events was gained through the analysis of the improved hypocenters. Overall, the thesis successfully employed HypoDD to improve the accuracy of earthquake hypocenter placements, therefore deepening our comprehension of the seismic properties and fault formations.

3. DISCUSSION

The utilization of InSAR techniques to analyze the surface deformation resulting from the Hatay earthquake on February 20, 2023, has yielded valuable knowledge on the seismic activity in the area. This discussion centers on the primary discoveries, the consequences of the outcomes, and the constraints faced throughout the investigation.

The InSAR study identified clear and specific patterns of surface deformation linked to the Hatay earthquake. The produced interferogram from the descending images exhibited distinct displacement fringes, suggesting significant ground motion. The deformation was mostly localized in the East Anatolian Fault Zone (EAFZ) and the Dead Sea Fault Zone (DSFZ), confirming the documented tectonic activity in these areas. The measured displacement reached a maximum of $\sim$ 17 cm in the LOS direction according to the analysis of decending data. This rate is comparable with the deformation results in the region (Mikhailov et al., 2023). The profile studies revealed different levels of distortion, with certain regions displaying more noticeable ground movement. The observed variance is most likely attributed to disparities in fault slip and the specific geological conditions of the area.

Implementing Atmospheric Phase Screen (APS) correction greatly enhanced the quality of the interferograms. The revised data exhibited less air interference, resulting in enhanced precision in measuring ground deformation. Our results indicate that it is significant to examine to include atmospheric influences in InSAR investigations in order to guarantee the accuracy and dependability of the outcomes.

Slip distribution refers to the spatial pattern of fault slip during an earthquake. The deformation model research yielded useful information into the spatial distribution of displacement along the fault plane. The deformation and relocated seismicity in the region revealed that most of the slip took place at shallow depths, which aligns with the surface deformation patterns that were observed.

The results of this study have important consequences for evaluating the risk of earthquakes in the area. The comprehensive cartography of surface deformation and distribution of slip provide vital insights into the dynamics of the EAFZ and DSFZ. This data may be utilized to enhance seismic hazard models and provide valuable insights for the creation of more efficient mitigation techniques.

The findings underscore the necessity for enhanced earthquake readiness in the Hatay region. The detected ground deformation and aftershock seismicity distribution indicate that forthcoming earthquakes have the potential to inflict substantial destruction, especially in regions experiencing severe deformation. This highlights the significance of enforcing strong construction regulations and emergency preparedness strategies to minimize the consequences of future seismic events.

This work showcases the efficacy of InSAR methods in monitoring and assessing surface deformation resulting from earthquakes. The effective implementation of APS correction and demonstrates the capability of these methods to offer precise and comprehensive data on seismic activity. Subsequent research endeavors might capitalize on these progressions to enhance the precision and dependability of InSAR assessments.

While the Sentinel-1 data offered vital information on the deformation patterns, its temporal resolution and coverage were restricted. Future research might be enhanced by including supplementary datasets that offer greater temporal resolution and broader coverage. This would lead to improved precision and comprehensiveness in the study of deformation.

4. CONCLUSION

This thesis has conducted a comprehensive examination of the surface displacement resulting from the Hatay earthquake on February 20, 2023, utilizing Interferometric Synthetic Aperture Radar (InSAR) methodologies. The study emphasizes the usefulness of InSAR in comprehending seismic activity and ground deformation, specifically in the intricate tectonic environment of the Anatolian Plate.

The InSAR research identified clear and specific surface deformation patterns linked to the Hatay earthquake. The produced interferograms exhibited distinct displacement fringes, suggesting significant ground motion. The deformation patterns were mostly localized at the East Anatolian Fault Zone (EAFZ) and the Dead Sea Fault Zone (DSFZ), confirming the documented tectonic activity in these areas.

The displacement measured reached a maximum of several centimeters, with notable variability among various profiles (Figure 2.14 and Figure 2.19). Profile investigations revealed different levels of distortion, Areas exhibiting more deformation were seen in close proximity to fault lines, where the slip was most pronounced.

Implementing Atmospheric Phase Screen (APS) correction enhanced the quality of the interferograms. The revised data demonstrated less air interference, resulting in more precise assessments of ground displacement. Applying APS correction was essential in separating the actual ground movement from air artifacts, which have the potential to greatly distort the InSAR results. This modification facilitated a more precise understanding of the co-seismic deformation.

The observed patterns of deformation and distribution of earthquakes in the region show a strong correlation with high Vp values at seismogenic depths in the region. The position and features of the Hatay earthquake align with the tectonic activity related to the EAFZ and DSFZ, which have previously caused important seismic events.

Understanding the historical context aids in comprehending the repetitive occurrence of seismic activity in the region.

The results of this study have important consequences for evaluating the risk of earthquakes in the Hatay region. Thoroughly measuring the surface deformation and improves our understanding of how the EAFZ and DSFZ behave. This is crucial for enhancing earthquake hazard models and creating effective ways to reduce their impact. Through the identification of places experiencing significant deformation, it becomes feasible to anticipate regions that are more susceptible to future seismic occurrences.

The findings emphasize the necessity for enhanced earthquake readiness in the Hatay region. Based on the observed ground deformation and seismicty patterns, it is evident that future earthquakes have the potential to cause substantial damage, especially in regions experiencing severe deformation. This highlights the significance of enforcing strong construction regulations and emergency preparedness strategies to mitigate the consequences of future earthquake occurrences. Targeted preparedness initiatives can provide significant benefits to communities located in high-risk locations.

Future research should prioritize efforts to overcome the mentioned constraints and investigate novel approaches to improve the precision and dependability of InSAR analysis. Possible approaches might involve the integration of InSAR data with other remote sensing technologies, enhancement of atmospheric correction techniques, and the refinement of slip models to accommodate intricate fault dynamics. Continued progress in these techniques is crucial for enhancing our capacity to efficiently observe and address seismic occurrences.

REFERENCES

1. Thatcher, W., "Interseismic Stress Recovery and the Earthquake Cycle in the North Anatolian Fault Zone", *Journal of Geophysical Research*, Vol. 111, No. B5, pp. 1-18, 2006.

2. Reid, H. F., *The Mechanics of the Earthquake*, Carnegie Institution of Washington, Washington, D.C., 1910.

3. Okay, A. I., Tüysüz, O., Kaya, S., "Tectonics of the North Anatolian Fault Zone", *Journal of Structural Geology*, Vol. 22, No. 6, pp. 837-857, 2000.

4. Reilinger, R., McClusky, S., Vernant, P., et al., "GPS Constraints on Continental Deformation in the Africa-Arabia-Eurasia Continental Collision Zone and Implications for the Dynamics of Plate Interactions", *Journal of Geophysical Research*, Vol. 111, No. B5, pp. 1-26, 2006.

5. Roukounakis, N., Elias, P., Briole, P., Katsanos, D. et al., "Tropospheric Correction of Sentinel-1 Synthetic Aperture Radar Interferograms Using a High-Resolution Weather Model Validated by GNSS Measurements", *Remote Sensing*, Vol. 13, No. 21, pp. 4342-4354, 2021.

6. Behera, A., Rawat, K. S., "A brief review paper on mining subsidence and its geoenvironmental impact", *Materials Today: Proceedings*, Vol. 51, pp. 1723-1731, 2023.

7. Hubert-Ferrari, A., King, G., Manighetti, I., Armijo, R., Meyer, B., Tapponnier, P., "Long-term elasticity in the continental lithosphere; modelling the Aden Ridge propagation and the Anatolian extrusion process", *Geophysical Journal International*, Vol. 153, No. 1, pp. 111-132, 2003.

8. Üneş, F., Kaya, Y. Z., "Evaluation of longterm air temperature, precipitation and flow rate parameters trend change using different approaches: a case study of Amik plain, Hatay", *Theoretical and Applied Climatology*, Vol. 143, No. 1, pp. 23-36, 2021.

9. Arslan, M. H., Dere, Y., Ecemis, A. S., Dogan, G., Ozturk, M., Korkmaz, S. Z., "Code-based damage assessment of existing precast industrial buildings following the February 6th, Kahramanmaraş earthquakes (Pazarcık Mw 7.7 and Elbistan Mw7.6)", *Journal of Building Engineering*, Vol. 46, Article 103718, 2024.

10. Cosca, M. A., Reid, M., Delph, J. R., Kuşcu Gonca, G. et al., "Age and mantle sources of Quaternary basalts associated with 'leaky' transform faults of the migrating Anatolia-Arabia-Africa triple junction", *Geosphere*, Vol. 16, No. 4, pp. 1035-1054, 2020.

11. Aldanmaz, E., "Geochemical constraints on the Cenozoic, OIB-type alkaline volcanic rocks of NW Turkey: Implications for mantle sources and melting processes", *LITHOS*, Vol. 86, No. 3-4, pp. 50-76, 2006.

12. Over, S., "Is the Amik Basin (SE Turkey) a triple-junction area? Analyses of SPOT XS imagery and seismicity", *International Journal of Remote Sensing*, Vol. 25, No. 22, pp. 4749-4764, 2004.

13. *Landscapes and Landforms of Turkey*, Springer Science and Business Media LLC, 2019.

14. Sezgin, S. K., Sakcalı, G. B., Özen, S., Yıldırım, E. et al., "Reconnaissance report on damage caused by the February 6, 2023, Kahramanmaraş Earthquakes in reinforced-concrete structures", *Journal of Building Engineering*, Vol. 46, Article 103719, 2024.

15. Ayso, E., Köz, İ., Doğanalp, S., Aslan, M., Tuşat, E., Kahveci, M., Taşpınar,

C., "Assessing the impact of the 2023 Kahramanmaraş and Hatay earthquakes on cadastre and property data using GPS and GIS", *Bulletin of Earthquake Engineering*, Vol. 22, No. 1, pp. 1-21, 2024.

16. Dwivedi, S. K., Hayashi, D., "Modeling the contemporary stress field and deformation pattern of eastern Mediterranean", *Journal of Earth Science*, Vol. 21, No. 1, pp. 13-25, 2010.

17. Huang, Q., "Precursory seismicity changes associated with the Mw= 7.4 1999 August 17 Izmit (Turkey) earthquake", *Geophysical Journal International*, Vol. 151, No. 3, pp. 661-672, 2002.

18. Kahraman, S., "A Comprehensive Health Economic Analysis of the 2023 Turkey Earthquake", *Disaster Medicine and Public Health Preparedness*, Vol. 17, No. 1, pp. 1-15, 2023.

19. Gürsoy, H., Piper, J. D. A., Tatar, O., Temiz, H., "A palaeomagnetic study of the Sivas Basin, central Turkey: Crustal deformation during lateral extrusion of the Anatolian Block", *Tectonophysics*, Vol. 271, No. 3-4, pp. 245-260, 1997.

20. Zuccolotto, G., "Assessing the Risk of Land Subsidence in the Lower Limpopo River Basin, Mozambique with Remote Sensing", Ph.D. Thesis, Duquesne University, 2023.

21. Mercimek, Ö., "Seismic Failure Modes of Masonry Structures Exposed to Kahramanmaraş Earthquakes (Mw 7.7 and 7.6) on February 6, 2023", *Engineering Failure Analysis*, Vol. 128, Article 105258, 2023.

22. Demirkesen, A. C., "Multi-risk interpretation of natural hazards for settlements of the Hatay province in the east Mediterranean region, Turkey using SRTM DEM", *Environmental Earth Sciences*, Vol. 66, No. 2, pp. 349-365, 2011.

23. Over, S., "Late Cenozoic stress distribution along the Misis Range in the Anatolian, Arabian, and African plate intersection region, SE Turkey", *Tectonics*, Vol. 23, No. 4, pp. 431-445, 2004.

24. Bağcı, U., Alpaslan, M., Frei, R., Kurt, M. A., Temel, A., "Different degrees of partial melting of the enriched mantle source for Plio-Quaternary basic volcanism, Toprakkale (Osmaniye) region, southern Turkey", *TÜBİTAK*, Vol. 25, No. 3, pp. 345-356, 2011.

25. Khair, K., Tsokas, G. N., Sawaf, T., "Crustal structure of the northern Levant region: multiple source Werner deconvolution estimates for Bouguer gravity anomalies", *Geophysical Journal International*, Vol. 129, No. 1, pp. 216-228, 1997.

26. Korkmaz, H., "Kahramanmaras Havzasi'nin Jeomorfolojisi", Ph.D. Thesis, Marmara Universitesi, 2021.

27. Taymaz, T., Ganas, A., Yolsal-Çevikbilen, S., Vera, F. et al., "Source Mechanism and Rupture Process of the 24 January 2020 Mw 6.7 Doğanyol–Sivrice Earthquake obtained from Seismological Waveform Analysis and Space Geodetic Observations on the East Anatolian Fault Zone (Turkey)", *Tectonophysics*, Vol. 784, pp. 126-137, 2021.

28. Westaway, R., "Kinematics of the Malatya–Ovacık Fault Zone", *Geodinamica Acta*, Vol. 14, No. 3-4, pp. 139-157, 2001.

29. Duman, T. Y., Robertson, A. H. F., Elmacı, H., Kara, M., "Palaeozoic-Recent geological development and uplift of the Amanos Mountains (S Turkey) in the critically located northwesternmost corner of the Arabian continent", *Geodinamica Acta*, Vol. 30, No. 3, pp. 171-190, 2017.

30. Gürbüz, A., "Tectonic Geomorphology of the North Anatolian Fault Zone in the Lake Sapanca Basin (eastern Marmara Region, Turkey)", *Geosciences Journal*,

Vol. 12, No. 4, pp. 327-335, 2008.

31. Bozkurt, E., "Neotectonics of Turkey – a synthesis", *Geodinamica Acta*, Vol. 14, No. 1-3, pp. 3-30, 2001.

32. Bayrak, E., Ozer, C., "The 24 January 2020 (Mw 6.8) Sivrice Elazig, Turkey earthquake: a first look at spatiotemporal distribution and triggering of aftershocks", *Arabian Journal of Geosciences*, Vol. 14, No. 1, pp. 3-16, 2021.

33. Ozener, H., "Kinematics of the eastern part of the North Anatolian Fault Zone", *Journal of Geodynamics*, Vol. 49, No. 4, pp. 1-17, 2010.

34. Gök, R., "Lithospheric structure of the continent collision zone: eastern Turkey", *Geophysical Journal International*, Vol. 170, No. 3, pp. 1055-1071, 2007.

35. İnce, Y., Kurnaz, T. F., "Probabilistic seismic hazard analysis of Kahramanmaras Province, Turkey", *Arabian Journal of Geosciences*, Vol. 11, No. 3, pp. 129-142, 2018.

36. McKenzie, D. P., "Active tectonics of the Mediterranean region", *Geophysical Journal International*, Vol. 30, No. 2, pp. 109-185, 1976.

37. Gülen, L., "The 1986 Koyulhisar earthquake sequence and its implications for fault mechanics and seismotectonics in the North Anatolian fault zone", *Journal of Geophysical Research*, Vol. 92, No. B7, pp. 5887-5901, 1987.

38. Karig, D. E., Kozlu, H., "Late Paleozoic and Mesozoic tectonic evolution of the Eastern Pontides, Turkey", *Tectonophysics*, Vol. 177, No. 1-3, pp. 213-228, 1990.

39. Perinçek, D., Çemen, I., "The role of strike-slip faults in the tectonic evolution of Southeastern Anatolia", *Geological Society of America Bulletin*, Vol. 102, No. 5,

pp. 724-746, 1990.

40. Westaway, R., Arger, J., "Kinematics of the Malatya-Ovacik fault zone", *Geodinamica Acta*, Vol. 9, No. 2, pp. 71-81, 1996.

41. Westaway, R., "Kinematics of the Malatya–Ovacık Fault Zone", *Geodinamica Acta*, Vol. 16, No. 3-4, pp. 183-203, 2003.

42. Khalifa, S., Mahdy, M., Hussein, H., Gomaa, M., "Implications of GPS-derived crustal deformation of the Sinai Peninsula, Egypt", *Arabian Journal of Geosciences*, Vol. 11, No. 3, pp. 429-442, 2018.

43. Arpat, E., Saroglu, F., "The East Anatolian fault system; thoughts on its development", *Maden Tetkik ve Arama Dergisi*, Vol. 79, No. 1, pp. 1-26, 1972.

44. Saroglu, F., Emre, O., Kuscu, I., "Active fault map of Turkey", *Maden Tetkik ve Arama Dergisi*, Vol. 84, No. 1, pp. 1-25, 1992.

45. Herece, E., Akay, E., "Doğu Anadolu fayı (DAF) atlası", *Maden Tetkik ve Arama Genel Müdürlüğü*, Vol. 92, No. 1, pp. 1-30, 2008.

46. Karabacak, V., Kadioglu, M., San, T., "Tectonic geomorphology of the North Anatolian Fault Zone in the Lake Sapanca Basin (eastern Marmara Region, Turkey)", *Geomorphology*, Vol. 122, No. 1-2, pp. 1-13, 2010.

47. Cetin, H., Guneyli, H., Mayer, L., "Paleoseismology of the Palu–Lake Hazar segment of the East Anatolian Fault Zone, Turkey", *Tectonophysics*, Vol. 453, No. 1-4, pp. 219-239, 2003.

48. Duman, T. Y., Emre, O., "The East Anatolian Fault: geometry, segmentation and jog characteristics", *Geological Society, London, Special Publications*, Vol. 372, No.

1, pp. 495-529, 2013.

49. Gülün, M., Yılmaz, A., Demir, N., "Seismic Risk Assessment and Management: Case Study of Istanbul", *Journal of Earthquake Engineering*, Vol. 11, No. 1, pp. 3-28, 1987.

50. Pirazzoli, P. A., Radtke, U., Hantoro, W. S., Jouannic, C., Hoang, C. T., Causse, C., Borel Best, M., "A One Million-Year-Long Sequence of Marine Terraces on Sumba Island, Indonesia", *Marine Geology*, Vol. 109, No. 3-4, pp. 221-236, 1993.